LA-UR-07-8410

*Approved for public release;
distribution is unlimited.*

Title: MCNP Generated Detector Response and Blur Functions for CsI Detectors

Author(s): Brian Temple

Intended for: MCNP references

Los Alamos NATIONAL LABORATORY
EST. 1943

MCNP Generated Detector Response and Blur Functions for CsI Detectors

Brian Temple

Abstract

MCNP simulations were performed using the *F8 tally to calculate the detector blur and detector response of a CsI detector. Different methods of representing the beam and tallying the energy deposition were explored for calculating blur functions for use in post-processing radiography simulations.

Introduction

The purpose of a scintillator in a detector is to convert higher energy photons from the radiograph into lower energy photons that are either read (absorbed) on film or converted into a charge that is read by electronics in order to obtain an image. The conversion of higher energy photons into lower energy photons involves a series of photon/electron chain reactions from the initial reaction of the incident photon with the scintillator. The chain reactions produce a number of secondary electrons and photons that spatially spreads out in the scintillator as more reactions occur. This spatial spread of the secondary photons is the blur that results from the scintillator. The blur is a function of the scintillator material, incident angle of the photon into the scintillator, and the energy of the photon. The amount of energy deposition in these chain reactions is proportional to the amount of lower energy photons produced. This relationship is used to determine the blur from the energy deposition calculated in the scintillator.

In MCNP radiography simulations the photon reactions in the scintillator are not explicitly modeled due to two main factors. First, the computational expense of trying to model the photon conversion in the scintillator is usually significant when compared to the expense of simulating the radiograph. Secondly, the physics in MCNP are not capable of modeling photons down to the low energies (less than 1 keV) measured on films or captured by imaging electronics.

The blur is incorporated into the simulations from pre-calculated information. Blur calculations are obtained from MCNP simulations by using the *F8 tally to calculate the energy deposition in concentric cylindrical cells from an incident beam of photons normal to the scintillator surface. The concentric cylindrical cells capture the radial distribution of the energy deposition. The radial contributions from all cells can be added together for each energy bin to give a detector response for the scintillator modeled. This summation of radial contributions gives a mapping function that correlates the tallied photon of a specific energy range to a corresponding energy deposition in the scintillator. Energy dependence can be modeled by calculating a single blur function using the entire spectrum of photons hitting the scintillator or by calculating multiple blur functions using discrete energies of photons over the entire spectral range of interest. While the detector response energy deposition corresponds to the number of lower energy photons created in the scintillator, it does not have any relationship to the spatial diffusion of photons in the scintillator. The spatial spread in the energy deposition is used to create a spatial blur function that is post-processed on the simulation data. This post-processing of a spatial blur decouples the energy dependency of the blur from its spatial distribution.

The angular dependence of the blur is not usually accounted for in blur calculations since it is too computationally expensive to break the incident photon energy deposition into energy, radial, and angular sets of information. Thus the incident photons in the calculations are normal to the surface of the scintillator. Some of the angular dependence of the incident photons on the scintillator can be captured in MCNP by using a FMESH tally plotted over the scintillator volume. This type of tally counts the path length of the photons traveling through the FMESH voxels. Photons entering the scintillator at an angle will have a shorter path length in the voxel than photons entering the scintillator at 90 degrees to the surface and can travel into neighboring voxels (see Figure 1). Angular trajectories into the scintillator are correctly weighed in the voxel, but the units of measurement are either particles/cm^2 or MeV/cm^2 which have no relationship to the energy deposition in the voxel. Thus the FMESH tally cannot capture all the physical properties of the blur.

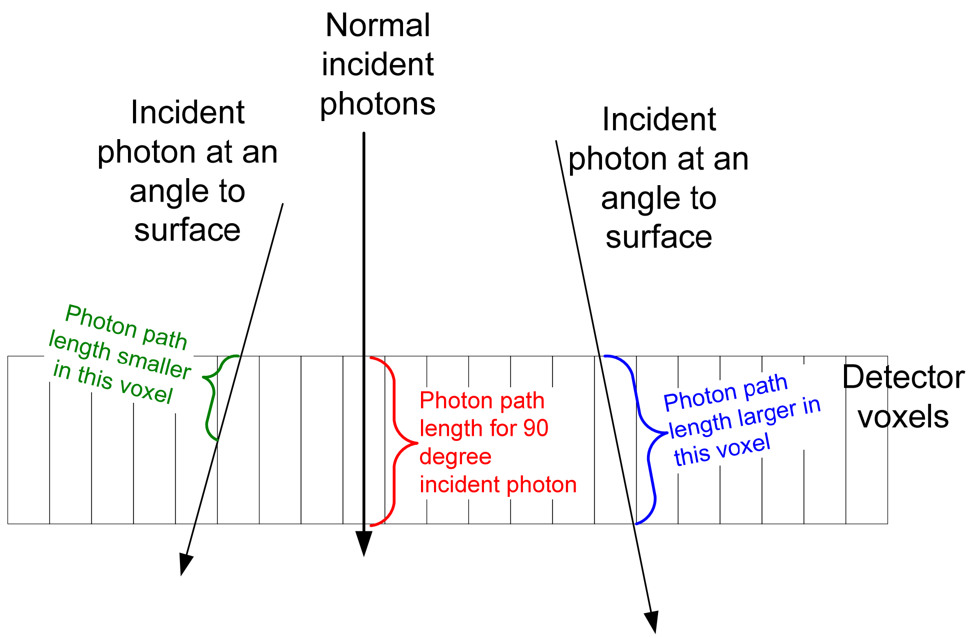

Figure 1 – Path lengths for different photon trajectories.

An artifact of spatially blurring the image after it has been tallied is the loss of the continuous spatial distribution of the blurring. If the photon’s trajectory is normal to the surface, the blurring is centered at the location of the photon entering the scintillator on average. In simulations the photons are counted across the front facial area of the pixels and their tally data is represented at a single location in the pixel (frequently it is the pixel center). When the pixelized data is blurred, the blur function acts on all photons counted in the pixel as if their location of incidence is the center of the pixel. Most pixels are rectangular or square, so any photons counted near a corner of the pixel are shifted to the center of the pixel and then diffused to the center of the neighboring pixels. The natural spatial diffusion of a photon entering the pixel near a corner is discretized into diffusion occurring from and to pixel centers.

Four types of detector blurring simulations were performed to try to account for the blurring that occurs in reality and the blurring that occurs in simulations. All calculations used a billion photons incident on the scintillator. Four different methods were used to calculate the detector blur for discrete energies ranging from 0-6 MeV. The energy bins are smallest below 300 keV and are increased in size gradually up to 6 MeV. Two different incident beam spatial distributions were used. A pencil beam distribution is used to correspond to individual photons incident on the scintillator. The other spatial distribution projects a square beam with a cross-section equal in area to a pixel onto the scintillator. This square beam shape reflects simulation image data that is discretized into uniform values across the pixels. Two different energy deposition tallies were also used. Concentric cylindrical cells that tally the energy deposition in radial bins are used in half the calculations. The other half tallies energy deposition in square pixel cells equal in size (0.035cm by 0.035cm) to the image pixels.

The simulations were run on the FLASH LINUX cluster computers. The executable used for the simulations was a beta version of MCNP6 code with a special FMESH cell tagging capability produced by Jeremy Sweezy. This executable has all the same run options as the default MCNP6 executable located in the /usr/projects/mcnp/ directory on FLASH.

Simulation methods

The four different methods were used to calculate detector blurs for the CsI detector composed of the material layers given in Figure 2. The front layer is 0.9cm of CsI followed by 0.0127cm of amorphous silicon. After the silicon layer is 0.1143cm of glass, followed by 0.254cm of aluminum.

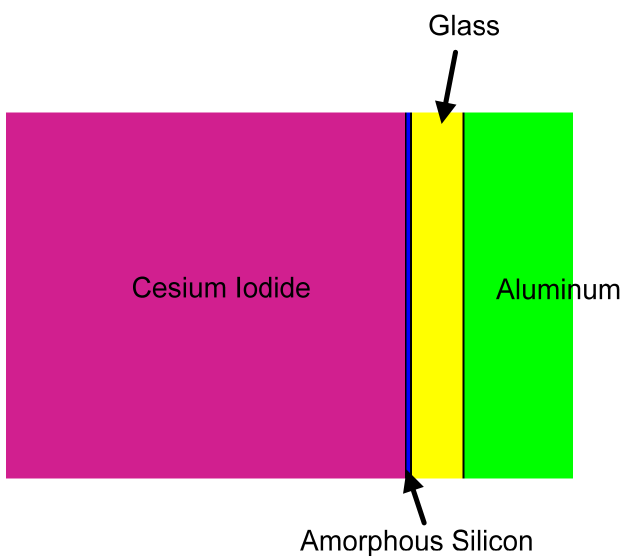

Figure 2 – Layers of the CsI detector.

The first set of simulations is named "pen_rad" and is the standard simulation technique used to calculate blur functions. This calculation reflects the spread of the incident photons in the scintillator *minus the angular effects from the photon trajectory into the CsI* and better represents real photon blur in an experiment. The pen_rad response was created from a pencil beam of photons striking the CsI scintillator normal to the surface at the center of the cylindrical tally cells. The energy deposition in the CsI is tallied in concentric cylindrical cells to measure the radial diffusion of the energy deposition. A schematic of the simulation is shown on the left side of Figure 3.

The second set of simulations is named “pix_rad” and has a photon beam with a cross-sectional area equal in area to the face of a pixel. The photons strike the scintillator at an angle normal to the surface and in the center of concentric cylindrical cells used to measure the energy deposition as a function of radius. The energy deposition is tallied in the same manner as the “pen_rad” method. Having the cross-sectional area of the photons equal to the facial area of a pixel is meant to represent the simulation image data that is uniform across the pixel. Using this beam rather than a pencil beam approximates the spatial distribution of counts across the entire pixel face as a constant value. The schematic for this method is given on the right side of Figure 3.

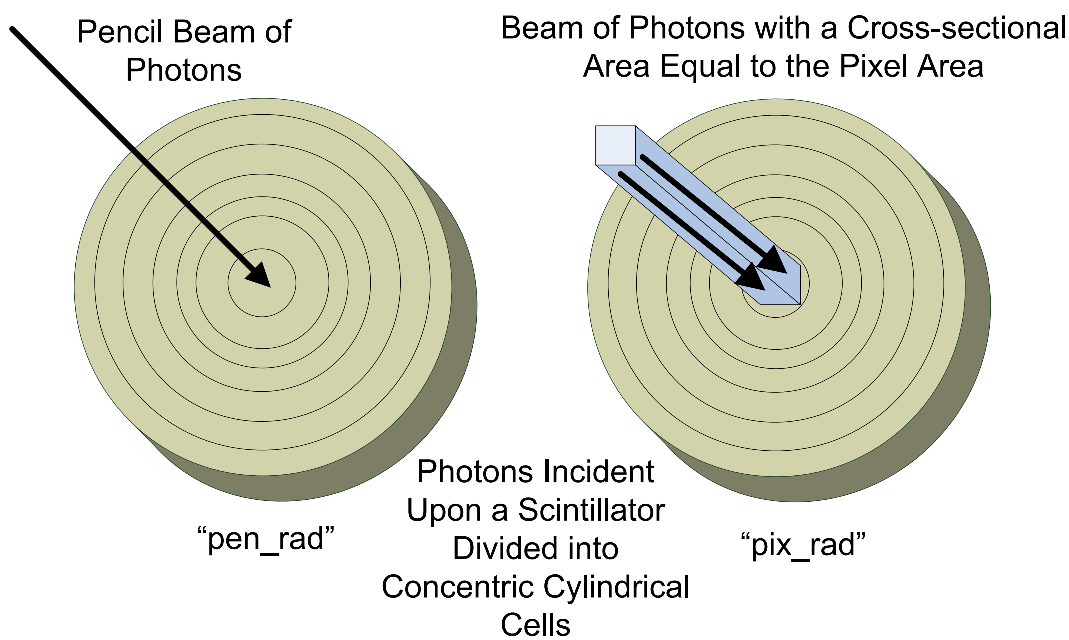

Figure 3 – Schematics of the “pen_rad” and “pix_rad” detector blur calculations.

The third set of simulations is named “pix_pix” and has a photon beam with a cross-sectional area equal in area to the face of the pixels. The photons strike the scintillator at an angle normal to the surface. The square photon beam approximates the spatial distribution of counts across the pixel center in the same manner as the “pix_rad” method. The energy deposition in the scintillator is tallied in neighboring pixels (pixels are made into cells) rather than radial cells to reflect the fact that the image data is divided into pixels. In simulations the blur diffuses from one pixel to another when post-processing the image. The distance from the center of the neighboring pixels to center pixel will be used to get the radial distance for the energy deposition for comparison with the first two methods. This means of tallying the energy deposition better reflects how blur is diffused from pixel to pixel when data is discretized. A schematic of the simulation is shown on the left side of Figure 4.

The fourth set of calculations is named "pen_pix" and has a pencil beam of photons normally incident on a set of square pixels used for tallying the energy deposition. Having the beam strike the center of a pixel shows how the blur will diffuse from the center of a pixel to neighboring pixel centers. This method reflects how blurring is actually performed when it is post-processed on discretized image data stored at the pixel centers. This method will have no pixel corner blurring effects and can be compared to the third method to provide an insight into the magnitude of corner blurring. A schematic of the method is given on the right side of Figure 4.

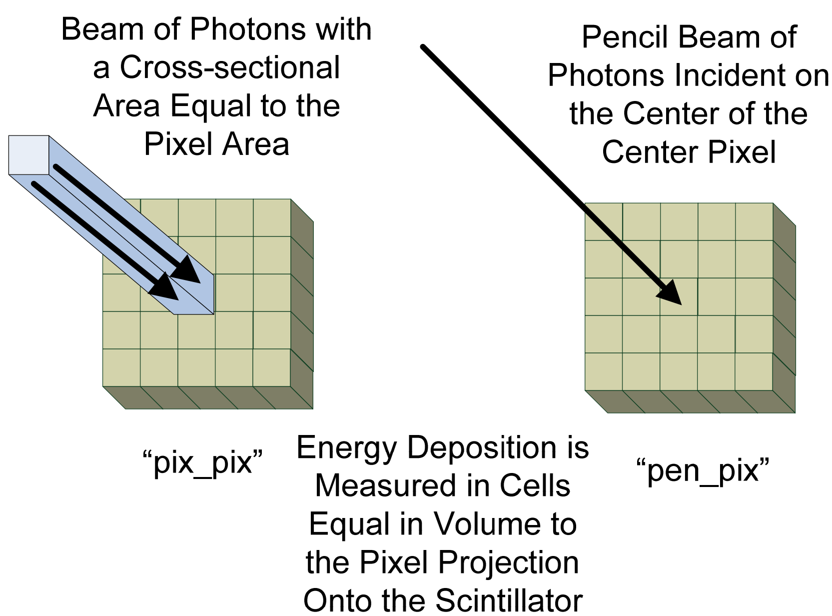

Figure 4 – Schematics of the "pix_pix" and "pen_pix" detector blur calculations.

Example MCNP input files are given in Appendix A. The "pen_rad" and "pix_pix" input files are provided to give inputs for the both sets of beam shapes and both types of energy deposition tallies. The sdef cards in each input file can be interchanged to get all four simulation methods.

Detector blur calculation results

The detector blur results for all methods are given in the four appendices at the end of the paper. Each appendix contains 3-D plots from two different software packages (JMP and EXCEL) to assist in the visualization of the blur. In the 3-D JMP plots the red data points are data for radii under 0.05 cm. The green data points are for data from 0.05-0.1cm radii. The blue data points are for data from radii 0.1cm to 0.2cm. The purple data points are for radii above 0.2cm. Appendix B contains the "pen_rad" plots in Figures 10-14. Appendix C contains the "pix_rad" plots in Figures 15-19. Appendix D contains the "pix_pix" plots in Figures 20-24. Appendix E contains the "pen_pix" plots in Figures 25-29.

All sets of three dimensional plots differ for each simulation method. All sets show the radial diffusion of the blur increasing for higher incident energies. The “pen_rad”, “pix_pix”, and “pen_pix” plots all peak at about the same amount at the same energy. The “pix_rad” peak is significantly lower. This difference can be explained by the incident beam area being spread over a several cells in the “pix_rad” case while all other sets have the incident photons striking the centermost tally cell only. Having the incident beam enter the scintillator across more than one cell has other effects on the energy deposition as seen in the detector response plots in Figure 5 and Figure 6. The detector response will be addressed in greater detail in the next section.

A discrepancy in the results is the different radial distribution for the “*_rad” results and the “*_pix” results. The “*_rad” results spatially drop off more gradually than the “*_pix” results. This is a function of the pixel cells being different in size and shape than the cylindrical cells. The amount of energy deposition to neighboring pixels is a partial function of the common surface area between the pixels and the volume of the pixel cell. The surface area between and the volume of concentric cylindrical cells increases as a function of radius and differs from the pixel cells. The cell volume is constant for pixel cells and the surface area between cells differs by the location of the neighboring cells around the center cell. These factors all contribute to the different radial diffusion profiles for the blur. The cylindrical cells do not have a larger volume than the pixel cells until a radius of 0.04 cm or larger. Likewise the cylindrical cell surface area with neighboring cells is not larger than the pixel cell surface area until a radius of 0.025 cm or larger. That difference contributes to the “*_pix” results having a larger energy deposition at shorter distances from the center that spatially falls off quicker. This difference in the radial distribution does not explain why the energy deposition for the “*_pix” methods is consistently lower than the “*_rad” results in Figures 5 and 6. We will explore the lower energy deposition results in greater detail in the next section.

The two closest matching plots are the “pix_pix” and the “pen_pix’ data. This consistency indicates that the using a pencil beam or a beam with a cross-sectional area equal to a pixel area does not significantly affect the blur or the energy deposition as long as the incident area of the beam is smaller than the cell boundaries. The results for the “*_pix” methods and the “pix_rad” method indicates that the biggest factor affecting the simulated blur appears to be the surface area of the incident beam being larger than the energy deposition cell area. We shall explore this discrepancy in greater detail by looking at the detector response for the four methods in the next section.

Detector response calculation results

Detector response functions can be obtained from the blur calculations by summing up all the radial contributions over the entire spatial region. The response functions for all the blur calculations are given in Figure 5 and Figure 6.

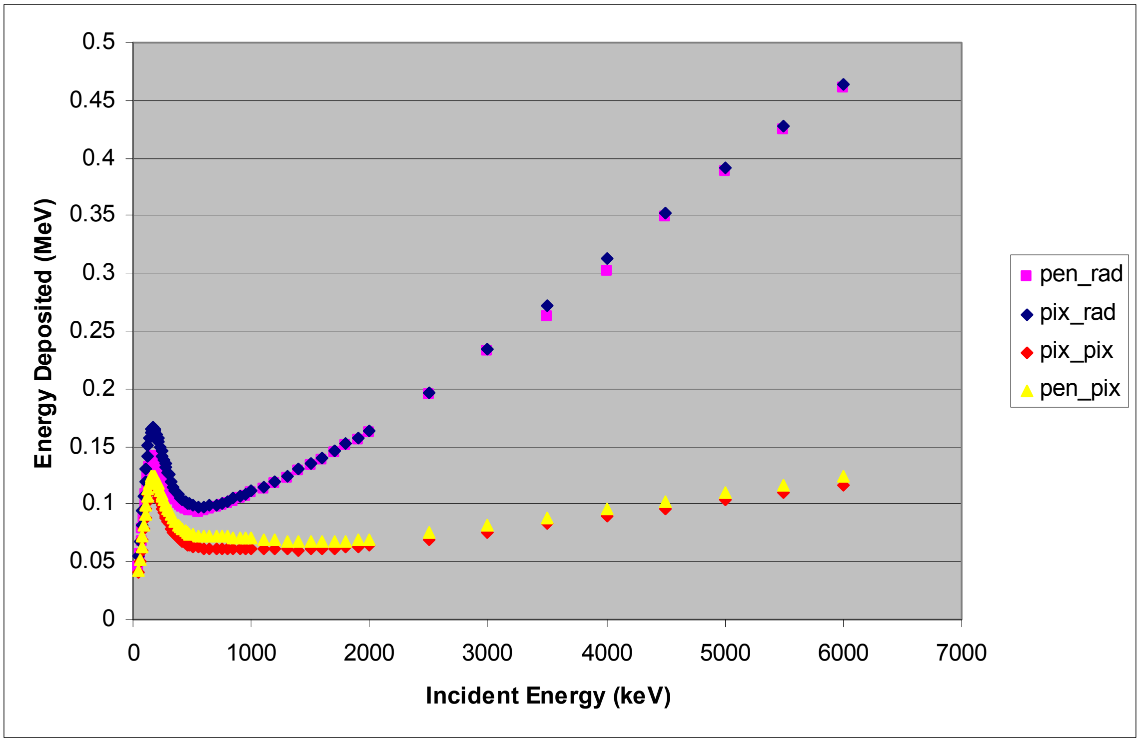

Figure 5 – Detector response for the CsI detector.

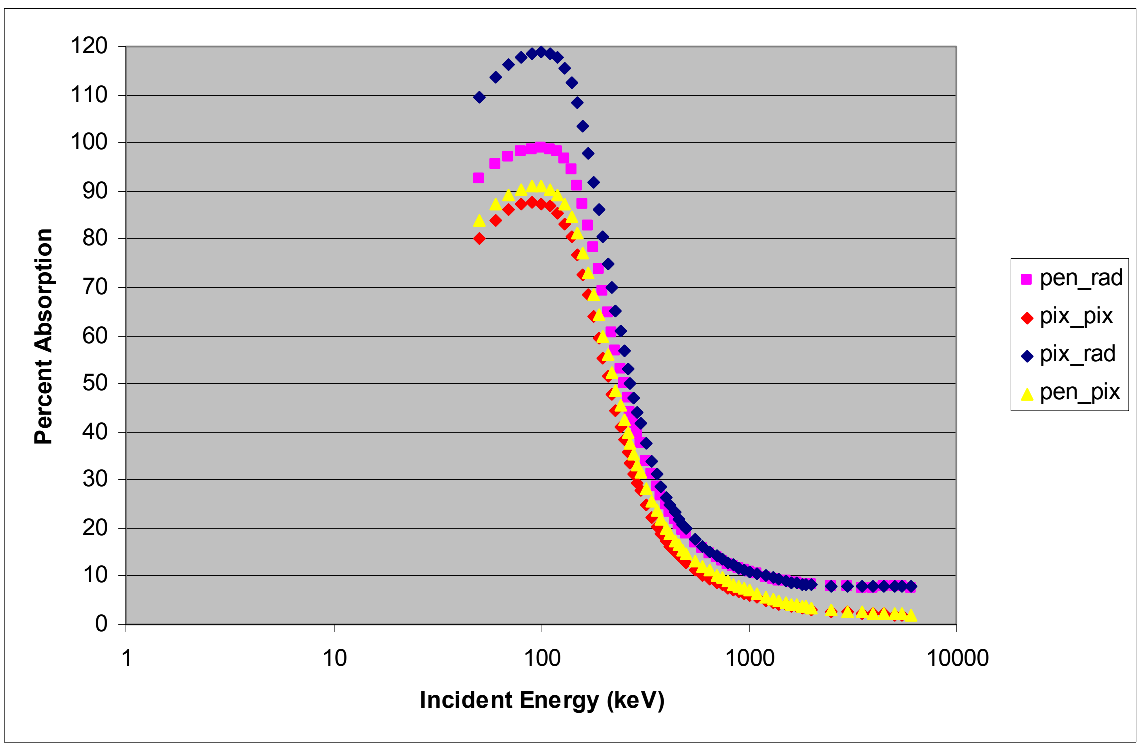

Figure 6 – CsI absorption efficiency for detector from detector blur simulations.

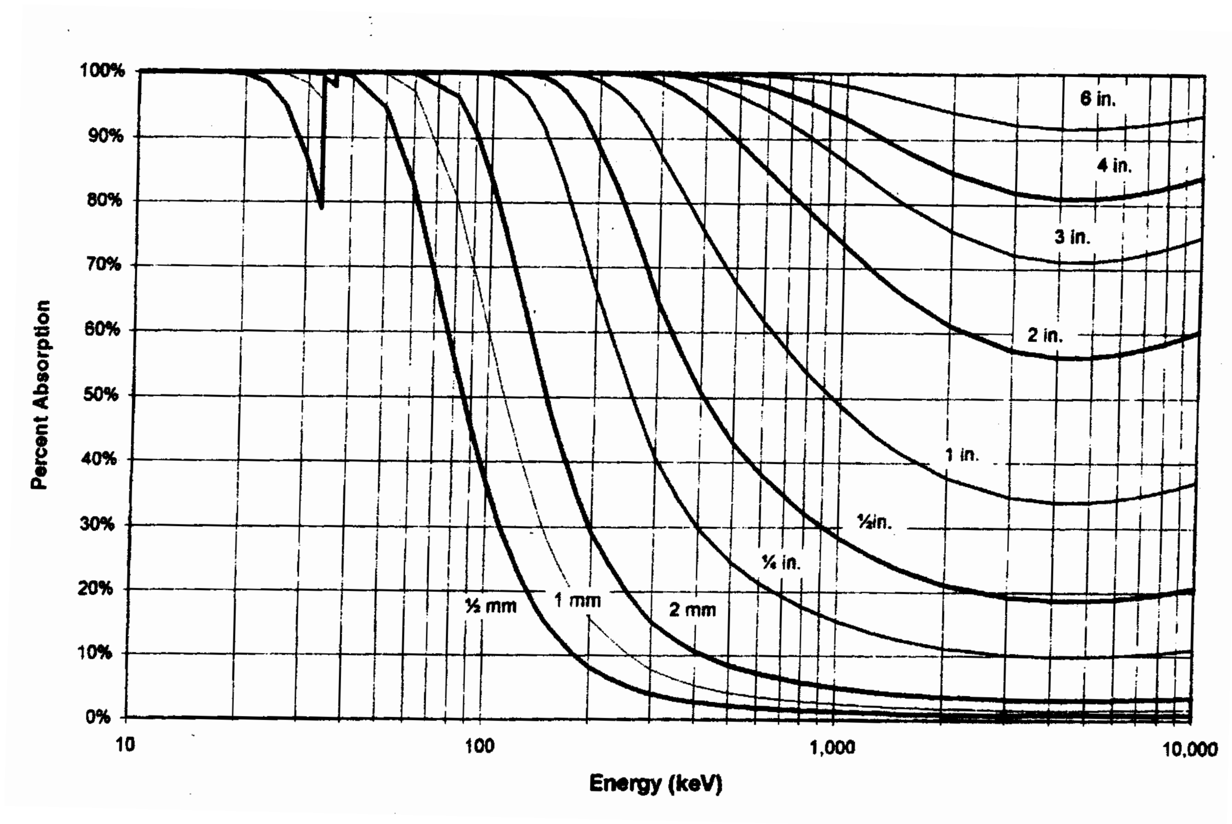

Figure 7 – Calculated Absorption efficiency for CsI from the Bicron manual.

The plot of the detector responses is shown as the energy deposited as a function of incident energy in Figure 5. In Figure 6 the same data is shown as the percentage of energy absorbed as a function of incident energy. The data in Figure 6 can be compared to the CsI response calculated for CsI only listed in the Bicron manual and shown in Figure 7.[1] In Figure 7 the percent absorption is $(I_0-I)/I_0$ where:

$$I = I_0 e^{-\mu x}$$

I_0 = Number of photons incident on material of thickness x
x = Thickness of material
I = Number of photons that have passed through material of thickness x
μ = Linear attenuation coefficient

The only response function that appears consistent with the analytical results in Figure 7 is the “pen_rad” results. The calculation for the 9mm thick scintillator peaks below 100% at around 100keV and plateaus at the higher energies at around 8%, which is similar to the ¼ in. (6.35mm) and the ½ in. (12.7mm) curves in Figure 7. The curve shapes are not exactly the same since the simulation uses full transport on all materials in detector, while the analytical results are only for CsI. The presence of the amorphous silicon, glass, and aluminum behind the CsI will affect the photon and electron absorption and scatter characteristics. The fact that we tallied energy deposition using radial cells rather than a linear deposition in slabs has no effect on the detector response because we are tallying the total energy deposited across the entire spatial region in both cases.

The differences between the analytical results and the other three simulation methods are puzzling. One significant problem seen in the detector response plots for the "pix_rad" method is the lack of energy conservation at lower energies. At 160 keV and below the "pix_rad" energy deposition is greater than the incident energy of the beam. The radial thicknesses of the cylindrical cells are small (less than a tenth of a millimeter) in the "*_rad" simulations. In the "pix_rad" case the beam has a cross-sectional area of 0.035 cm by 0.035 cm and covers over the first five concentric cylindrical cells out to a radius of 0.02475 cm. This broader deposition area is seen in the "pix_rad" detector blur plots in Figures 15-17 in Appendix C. In the other cases the incident beam hits the scintillator at the centermost tally cell only. The broad deposition of incident photons across multiple cells increases the spread of photons (and their subsequent electrons) across the cells and appears to worsen the energy conservation problem.

Another big problem is with the "*_pix" results having lower total energy deposition than the "*_rad" results using concentric cylindrical cells. Both sets of simulations should give the same total energy deposited since the sum of their cells measures around the same total volume. In the three dimensional radial plots in the last four appendices, the radial energy distribution falls of significantly within a millimeter of the incident cell radius for lower incident energies. Thus the volumes covered by the concentric cylindrical cells and the pixel cells are more than adequate to capture nearly all the energy deposition and avoid edge losses at lower energies. Only the highest incident energy photons deposit energy at larger radii and could have edge losses. Yet the pixel cells have a consistently lower total energy deposition than the concentric cylindrical cells for all energy ranges.

It was suggested that the energy-straggling model used in the simulations be investigated.[2,3] The MCNP calculations used full photon-electron transport down to a cut-off energy of 10 keV and used the *F8 tally for counting the cell energy deposition. Statements in the MCNP manual on the idiosyncrasies of the *F8 tally describe energy conservation issues with the tally. The problem occurs mainly with electrons that have mean free path's larger than the tally cell dimensions. A correction to the energy straggling model in the code was made by Grady Hughes, but this option was not available in the executable used when these calculations were begun.

Five sets of additional calculations were performed for energies from 50-200 keV to verify if the energy straggling issue across cells is a problem. First the "pix_rad" calculations were repeated with the Hughes energy straggling model turned on ("pix_rad_H"). Next the energy deposition for the pencil beam and pixel area beam were replicated using a single large cylindrical tally cell equal in volume to the multiple cylindrical cells used before ("pen_one" and "pix_one"). Next the Hughes energy straggling was used with a pixel area beam incident on a single large cylindrical tally cell equal in volume to the multiple cells used before ("pix_H_1"). Finally the "pix_rad" simulations using the Hughes energy straggling model run option ("pix_rad_H" results) were repeated using the default MCNP6 executable located in the /usr/projects/mcnp/

directory on FLASH. The default executable and the Sweezy MCNP6 beta version executable gave identical results. The results for the first four sets of additional simulations along with the original simulation results in the same energy range are given in Figure 8 and Figure 9.

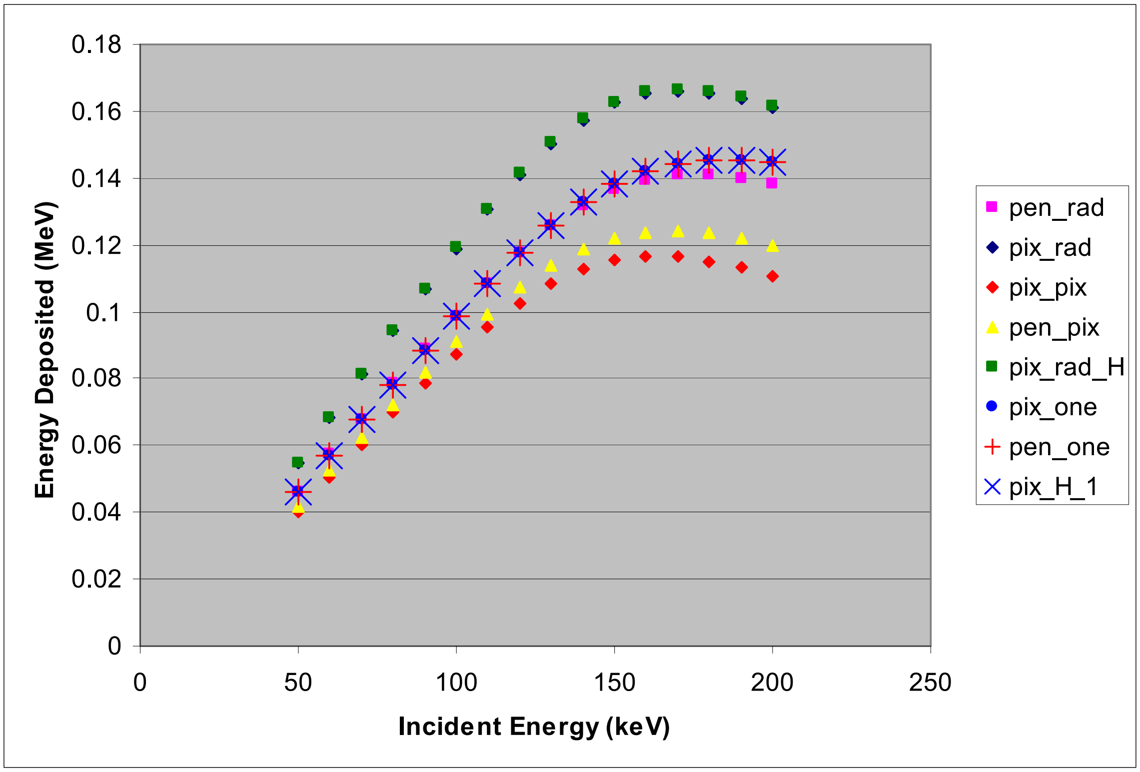

Figure 8 – Detector response for the CsI detector from 50-200keV.

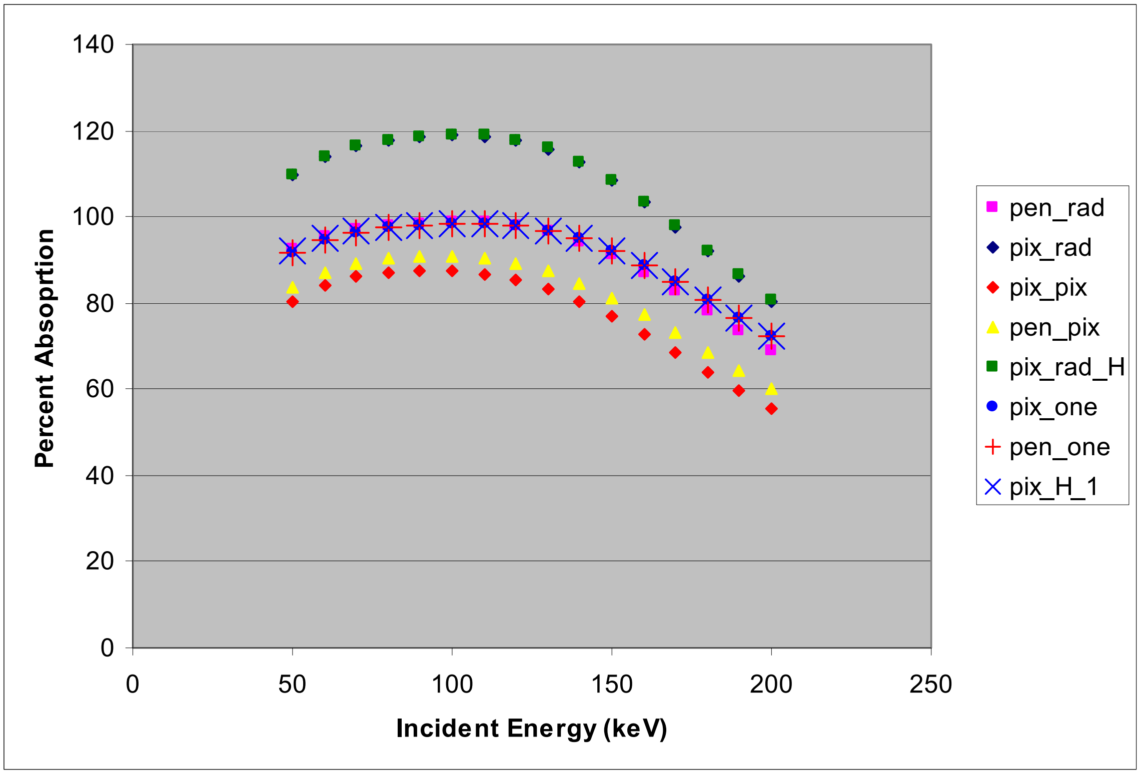

Figure 9 – Percent absorption for the CsI detector from 50-200keV.

The addition of the Hughes energy straggling model did nothing to correct the energy conservation problem with the pixel area beam. The "pix_rad_H" response data points lay nearly on top of the "pix_rad" results. The substitution of the multiple energy deposition cells with the single cell gave consistent results for all simulations regardless of the beam area used or the addition of the Hughes energy straggling. The use of a single energy deposition cell gave energy conservation for all beam shapes and energy straggling models. As the incident energy increases beyond 150 keV, the "pen_rad" results start to diverge from the single cell results. All of the "*_pix" results are different from the single cell results. These discrepancies for different multiple cell tallies suggest that there is a transport issue across cell boundaries with the *F8 tally.

Speculation arose that the "knock-on" electron problems addressed in the MCNP manual was another problem.[3] The number of "knock-ons" listed in the MCNP outp files for the simulations are given in the table below for the 80 keV and 150 keV results.

	80 keV	150 keV
"pix_rad_H'	139366597	501181692
"pix_one"	176056701	613395253
"pix_rad"	175911508	612447437
"pen_one"	176048873	613423998
"pen_rad"	176023642	613216973

The only difference seen in the "knock-on" electron amount is between the simulations with and without the Hughes energy straggling. As seen in Figure 8 and Figure 9 the energy-straggling model had minimal effect on the response results. The consistency of the 'knock-on" values for the single cell and multiple cell simulations suggest that the "knock-on" electron problem in the code is not the problem for these energy deposition results.

Conclusions

The general 3-D shape from all detector blur simulations verifies that the blur is a function of the incident photon energy. The discrepancy in the blur shapes is a result of using different cell shapes to measure the energy deposition and different incident beam shapes. The lack of consistency for the detector response results indicates a deeper problem with the *F8 tally across cell boundaries. The consistency of the single cell results and the disparity in the multiple cell results show the discrepancies in energy deposition to be related to the transport of the energy deposition across cell boundaries and the application of the incident beam across multiple cell surfaces. Further investigation of these issues is required by the Eolus team.

It is recommended at this time that the "pen_rad" method be the method used for calculating blur functions. This method has the most consistent detector response results with the single cell tally data and the analytical calculations. All four methods should be compared again once the issues presented above have been addressed.

Appendix A

"pen_rad" method MCNP input file

```
C  CsI ptspr using 6x cylinders
C @@@  ENERGY = 0.05 0.06 0.07 0.08 0.09 0.10
c
1 0       2 -4 -1
20 3 -4.51 4 -5 -70
21 3 -4.51 4 -5 70 -71
22 3 -4.51 4 -5 71 -72
23 3 -4.51 4 -5 72 -73
24 3 -4.51 4 -5 73 -74
25 3 -4.51 4 -5 74 -75
26 3 -4.51 4 -5 75 -76
27 3 -4.51 4 -5 76 -77
28 3 -4.51 4 -5 77 -78
29 3 -4.51 4 -5 78 -79
30 3 -4.51 4 -5 -10 79
31 3 -4.51 4 -5 10 -11
32 3 -4.51 4 -5 11 -12
33 3 -4.51 4 -5 12 -13
34 3 -4.51 4 -5 13 -14
35 3 -4.51 4 -5 14 -15
36 3 -4.51 4 -5 15 -16
37 3 -4.51 4 -5 16 -17
38 3 -4.51 4 -5 17 -18
39 3 -4.51 4 -5 18 -19
40 3 -4.51 4 -5 19 -20
41 3 -4.51 4 -5 20 -21
42 3 -4.51 4 -5 21 -22
43 3 -4.51 4 -5 22 -23
44 3 -4.51 4 -5 23 -24
131 3 -4.51 4 -5 24 -25
132 3 -4.51 4 -5 25 -26
133 3 -4.51 4 -5 26 -27
134 3 -4.51 4 -5 27 -28
135 3 -4.51 4 -5 28 -29
136 3 -4.51 4 -5 29 -30
137 3 -4.51 4 -5 30 -31
138 3 -4.51 4 -5 31 -32
139 3 -4.51 4 -5 32 -33
140 3 -4.51 4 -5 33 -34
141 3 -4.51 4 -5 34 -35
142 3 -4.51 4 -5 35 -36
143 3 -4.51 4 -5 36 -37
144 3 -4.51 4 -5 37 -38
145 3 -4.51 4 -5 38 -39
146 3 -4.51 4 -5 39 -40
147 3 -4.51 4 -5 40 -41
148 3 -4.51 4 -5 41 -42
149 3 -4.51 4 -5 42 -43
150 3 -4.51 4 -5 43 -44
151 3 -4.51 4 -5 44 -45
152 3 -4.51 4 -5 45 -46
153 3 -4.51 4 -5 46 -47
154 3 -4.51 4 -5 47 -48
```

```
155 3 -4.51 4 -5 48 -49
156 3 -4.51 4 -5 49 -50
157 3 -4.51 4 -5 50 -51
158 3 -4.51 4 -5 51 -52
159 3 -4.51 4 -5 52 -53
160 3 -4.51 4 -5 53 -54
161 3 -4.51 4 -5 54 -55
162 3 -4.51 4 -5 55 -56
163 3 -4.51 4 -5 56 -57
164 3 -4.51 4 -5 57 -58
165 3 -4.51 4 -5 58 -59
166 3 -4.51 4 -5 59 -60
167 3 -4.51 4 -5 60 -61
168 3 -4.51 4 -5 61 -62
169 3 -4.51 4 -5 62 -63
170 3 -4.51 4 -5 63 -1
901 4 -2.35 5 -6 -1
902 5 -2.18 6 -7 -1
903 6 -2.70 7 -8 -1
7 0 8:-2:1

c surface cards
1010 cx 1.e-05
1 cx 10
2 px -3.2532
4 px 0.0
5 px 0.9     $ scintillator is 9 mm thick
6 px 0.9127  $ amorphous silicon is 0.0127 cm
7 px 1.0270  $ glass thickness 0.1143 cm
8 px 1.2810  $ aluminum thickness 0.254 cm
70 cx .005
71 cx .010
72 cx .015
73 cx .020
74 cx .025
75 cx .030
76 cx .035
77 cx .040
78 cx .045
79 cx .050
10 cx .055
11 cx .060
12 cx .065
13 cx .070
14 cx .075
15 cx .080
16 cx .085
17 cx .090
18 cx .095
19 cx .100
20 cx .105
21 cx .110
22 cx .115
23 cx .120
24 cx .125
25 cx .130
26 cx .135
```

```
27 cx .140
28 cx .145
29 cx .150
30 cx .155
31 cx .160
32 cx .165
33 cx .170
34 cx .175
35 cx .180
36 cx .185
37 cx .190
38 cx .195
39 cx .200
40 cx .205
41 cx .210
42 cx .215
43 cx .220
44 cx .225
45 cx .230
46 cx .235
47 cx .240
48 cx .245
49 cx .250
50 cx .255
51 cx .260
52 cx .265
53 cx .270
54 cx .275
55 cx .280
56 cx .285
57 cx .290
58 cx .295
59 cx .300
60 cx .305
61 cx .310
62 cx .315
63 cx .320

c physics cards
cut:p j 0.010
cut:e j 0.010
phys:p 2j 1
imp:p 1 68r 0
imp:e 1 68r 0
mode p e
c
m2 71000 2 14000 1 8016 5
c m3 80000 1 53000 2    $ Mercury Iodide HgI2 rho = 6.36 g/cm3
m3 55000 1 53000 1    $ Cesium Iodide rho = 4.51 g/cm3
m4 14000 2 1001 6     $ Amorphous silicon rho = 2.35 g/cc
m5 14000 1 8000 2     $ glass rho = 2.18 g/cc
m6 13000 1              $aluminum rho = 2.70 g/cc
c
sdef dir=1 vec=1 0 0 pos -3.2532 0 0  erg=ENERGY
c
c tallies
f1:p 4
```

```
c1 0. 1.
c above is a probab check to make sure nothing is lost
c
c Charge deposition
+f8:pe 20 21 22 23 23 25 26 27 28 29
       30 31 32 33 34 35 36 37 38 39 40 41 42 43 44 131
       132 133 134 135 136 137 138 139 140 141 142 143 144 145
       146 147 148 149 150 151 152 153 154 155 156 157 158 159 160
       161 162 163 164 165 166 167 168 169 170 t
c
c Energy deposition
*f18:pe 20 21 22 23 23 25 26 27 28 29
       30 31 32 33 34 35 36 37 38 39 40 41 42 43 44 131
       132 133 134 135 136 137 138 139 140 141 142 143 144 145
       146 147 148 149 150 151 152 153 154 155 156 157 158 159 160
       161 162 163 164 165 166 167 168 169 170 t
nps 1e9
prdmp 2j 1
```

"pix_pix" method MCNP input file

```
CsI ptspr using 6x cylinders
c
1 0  2 -4 -1  $ (1)
c
100 3 -4.51  4 -5 -1  10
       501 502 503 504 505 506 507 508 509 510
       511 512 513 514 515 516 517 518 519 520
       521 522 523 524 525 526 527 528 529 530
       531 532 533 534 535 536 537 538 539 540    $(2)
c
11  3 -4.51 4 -5  -11      $ (3)
c
101 3 -4.51 4 -5  -101     $ (4)
102 3 -4.51 4 -5  -102
103 3 -4.51 4 -5  -103
104 3 -4.51 4 -5  -104
105 3 -4.51 4 -5  -105
106 3 -4.51 4 -5  -106
107 3 -4.51 4 -5  -107
108 3 -4.51 4 -5  -108     $(11)
c
201 3 -4.51 4 -5  -201     $(12)
202 3 -4.51 4 -5  -202
203 3 -4.51 4 -5  -203
204 3 -4.51 4 -5  -204
205 3 -4.51 4 -5  -205
206 3 -4.51 4 -5  -206
207 3 -4.51 4 -5  -207
208 3 -4.51 4 -5  -208
209 3 -4.51 4 -5  -209
210 3 -4.51 4 -5  -210
211 3 -4.51 4 -5  -211
212 3 -4.51 4 -5  -212
213 3 -4.51 4 -5  -213
```

```
214 3 -4.51 4 -5  -214
215 3 -4.51 4 -5  -215
216 3 -4.51 4 -5  -216     $(27)
c
301 3 -4.51 4 -5  -301     $(28)
302 3 -4.51 4 -5  -302
303 3 -4.51 4 -5  -303
304 3 -4.51 4 -5  -304
305 3 -4.51 4 -5  -305
306 3 -4.51 4 -5  -306
307 3 -4.51 4 -5  -307
308 3 -4.51 4 -5  -308
309 3 -4.51 4 -5  -309
310 3 -4.51 4 -5  -310
311 3 -4.51 4 -5  -311
312 3 -4.51 4 -5  -312
313 3 -4.51 4 -5  -313
314 3 -4.51 4 -5  -314
315 3 -4.51 4 -5  -315
316 3 -4.51 4 -5  -316
317 3 -4.51 4 -5  -317
318 3 -4.51 4 -5  -318
319 3 -4.51 4 -5  -319
320 3 -4.51 4 -5  -320
321 3 -4.51 4 -5  -321
322 3 -4.51 4 -5  -322
323 3 -4.51 4 -5  -323
324 3 -4.51 4 -5  -324    $(51)
c
401 3 -4.51 4 -5  -401    $(52)
402 3 -4.51 4 -5  -402
403 3 -4.51 4 -5  -403
404 3 -4.51 4 -5  -404
405 3 -4.51 4 -5  -405
406 3 -4.51 4 -5  -406
407 3 -4.51 4 -5  -407
408 3 -4.51 4 -5  -408
409 3 -4.51 4 -5  -409
410 3 -4.51 4 -5  -410
411 3 -4.51 4 -5  -411
412 3 -4.51 4 -5  -412
413 3 -4.51 4 -5  -413
414 3 -4.51 4 -5  -414
415 3 -4.51 4 -5  -415
416 3 -4.51 4 -5  -416
417 3 -4.51 4 -5  -417
418 3 -4.51 4 -5  -418
419 3 -4.51 4 -5  -419
420 3 -4.51 4 -5  -420
421 3 -4.51 4 -5  -421
422 3 -4.51 4 -5  -422
423 3 -4.51 4 -5  -423
424 3 -4.51 4 -5  -424
425 3 -4.51 4 -5  -425
426 3 -4.51 4 -5  -426
427 3 -4.51 4 -5  -427
428 3 -4.51 4 -5  -428
```

```
429 3 -4.51 4 -5  -429
430 3 -4.51 4 -5  -430
431 3 -4.51 4 -5  -431
432 3 -4.51 4 -5  -432    $(83)
c
501 3 -4.51 4 -5  -501    $(84)
502 3 -4.51 4 -5  -502
503 3 -4.51 4 -5  -503
504 3 -4.51 4 -5  -504
505 3 -4.51 4 -5  -505
506 3 -4.51 4 -5  -506
507 3 -4.51 4 -5  -507
508 3 -4.51 4 -5  -508
509 3 -4.51 4 -5  -509
510 3 -4.51 4 -5  -510
511 3 -4.51 4 -5  -511
512 3 -4.51 4 -5  -512
513 3 -4.51 4 -5  -513
514 3 -4.51 4 -5  -514
515 3 -4.51 4 -5  -515
516 3 -4.51 4 -5  -516
517 3 -4.51 4 -5  -517    $(100)
518 3 -4.51 4 -5  -518
519 3 -4.51 4 -5  -519
520 3 -4.51 4 -5  -520
521 3 -4.51 4 -5  -521
522 3 -4.51 4 -5  -522
523 3 -4.51 4 -5  -523
524 3 -4.51 4 -5  -524
525 3 -4.51 4 -5  -525
526 3 -4.51 4 -5  -526
527 3 -4.51 4 -5  -527
528 3 -4.51 4 -5  -528
529 3 -4.51 4 -5  -529
530 3 -4.51 4 -5  -530
531 3 -4.51 4 -5  -531
532 3 -4.51 4 -5  -532
533 3 -4.51 4 -5  -533
534 3 -4.51 4 -5  -534
535 3 -4.51 4 -5  -535
536 3 -4.51 4 -5  -536
537 3 -4.51 4 -5  -537
538 3 -4.51 4 -5  -538
539 3 -4.51 4 -5  -539
540 3 -4.51 4 -5  -540   $(123)
c
901 4 -2.35 5 -6 -1      $(124)
902 5 -2.18 6 -7 -1
903 6 -2.70 7 -8 -1
7 0 8:-2:1               $(127)

c surface cards
1010 cx 1.e-05
1 cx 10
2 px -3.2532
4 px 0.0
5 px 0.9     $ scintillator is 9 mm thick
```

```
6 px 0.9127  $ amorphous silicon is 0.0127 cm
7 px 1.0270  $ glass thickness 0.1143 cm
8 px 1.2810  $ aluminum thickness 0.254 cm
c
10 rpp   0 0.9  -0.1925  0.1925  -0.1925  0.1925
c
11  rpp  0 0.9  -0.0175  0.0175  -0.0175  0.0175
c
101 rpp  0 0.9   0.0175  0.0525  -0.0525 -0.0175
102 rpp  0 0.9   0.0175  0.0525  -0.0175  0.0175
103 rpp  0 0.9   0.0175  0.0525   0.0175  0.0525
104 rpp  0 0.9  -0.0175  0.0175   0.0175  0.0525
105 rpp  0 0.9  -0.0525 -0.0175   0.0175  0.0525
106 rpp  0 0.9  -0.0525 -0.0175  -0.0175  0.0175
107 rpp  0 0.9  -0.0525 -0.0175  -0.0525 -0.0175
108 rpp  0 0.9  -0.0175  0.0175  -0.0525 -0.0175
c
201 rpp  0 0.9   0.0525  0.0875  -0.0875 -0.0525
202 rpp  0 0.9   0.0525  0.0875  -0.0525 -0.0175
203 rpp  0 0.9   0.0525  0.0875  -0.0175  0.0175
204 rpp  0 0.9   0.0525  0.0875   0.0175  0.0525
205 rpp  0 0.9   0.0525  0.0875   0.0525  0.0875
206 rpp  0 0.9   0.0175  0.0525   0.0525  0.0875
207 rpp  0 0.9  -0.0175  0.0175   0.0525  0.0875
208 rpp  0 0.9  -0.0525 -0.0175   0.0525  0.0875
209 rpp  0 0.9  -0.0875 -0.0525   0.0525  0.0875
210 rpp  0 0.9  -0.0875 -0.0525   0.0175  0.0525
211 rpp  0 0.9  -0.0875 -0.0525  -0.0175  0.0175
212 rpp  0 0.9  -0.0875 -0.0525  -0.0525 -0.0175
213 rpp  0 0.9  -0.0875 -0.0525  -0.0875 -0.0525
214 rpp  0 0.9  -0.0525 -0.0175  -0.0875 -0.0525
215 rpp  0 0.9  -0.0175  0.0175  -0.0875 -0.0525
216 rpp  0 0.9   0.0175  0.0525  -0.0875 -0.0525
c
301 rpp  0 0.9   0.0875  0.1225  -0.1225 -0.0875
302 rpp  0 0.9   0.0875  0.1225  -0.0875 -0.0525
303 rpp  0 0.9   0.0875  0.1225  -0.0525 -0.0175
304 rpp  0 0.9   0.0875  0.1225  -0.0175  0.0175
305 rpp  0 0.9   0.0875  0.1225   0.0175  0.0525
306 rpp  0 0.9   0.0875  0.1225   0.0525  0.0875
307 rpp  0 0.9   0.0875  0.1225   0.0875  0.1225
308 rpp  0 0.9   0.0525  0.0875   0.0875  0.1225
309 rpp  0 0.9   0.0175  0.0525   0.0875  0.1225
310 rpp  0 0.9  -0.0175  0.0175   0.0875  0.1225
311 rpp  0 0.9  -0.0525 -0.0175   0.0875  0.1225
312 rpp  0 0.9  -0.0875 -0.0525   0.0875  0.1225
313 rpp  0 0.9  -0.1225 -0.0875   0.0875  0.1225
314 rpp  0 0.9  -0.1225 -0.0875   0.0525  0.0875
315 rpp  0 0.9  -0.1225 -0.0875   0.0175  0.0525
316 rpp  0 0.9  -0.1225 -0.0875  -0.0175  0.0175
317 rpp  0 0.9  -0.1225 -0.0875  -0.0525 -0.0175
318 rpp  0 0.9  -0.1225 -0.0875  -0.0875 -0.0525
319 rpp  0 0.9  -0.1225 -0.0875  -0.1225 -0.0875
320 rpp  0 0.9  -0.0875 -0.0525  -0.1225 -0.0875
321 rpp  0 0.9  -0.0525 -0.0175  -0.1225 -0.0875
322 rpp  0 0.9  -0.0175  0.0175  -0.1225 -0.0875
323 rpp  0 0.9   0.0175  0.0525  -0.1225 -0.0875
```

```
324 rpp  0 0.9   0.0525  0.0875  -0.1225 -0.0875
c
401 rpp  0 0.9   0.1225  0.1575  -0.1575 -0.1225
402 rpp  0 0.9   0.1225  0.1575  -0.1225 -0.0875
403 rpp  0 0.9   0.1225  0.1575  -0.0875 -0.0525
404 rpp  0 0.9   0.1225  0.1575  -0.0525 -0.0175
405 rpp  0 0.9   0.1225  0.1575  -0.0175  0.0175
406 rpp  0 0.9   0.1225  0.1575   0.0175  0.0525
407 rpp  0 0.9   0.1225  0.1575   0.0525  0.0875
408 rpp  0 0.9   0.1225  0.1575   0.0875  0.1225
409 rpp  0 0.9   0.1225  0.1575   0.1225  0.1575
410 rpp  0 0.9   0.0875  0.1225   0.1225  0.1575
411 rpp  0 0.9   0.0525  0.0875   0.1225  0.1575
412 rpp  0 0.9   0.0175  0.0525   0.1225  0.1575
413 rpp  0 0.9  -0.0175  0.0175   0.1225  0.1575
414 rpp  0 0.9  -0.0525 -0.0175   0.1225  0.1575
415 rpp  0 0.9  -0.0875 -0.0525   0.1225  0.1575
416 rpp  0 0.9  -0.1225 -0.0875   0.1225  0.1575
417 rpp  0 0.9  -0.1575 -0.1225   0.1225  0.1575
418 rpp  0 0.9  -0.1575 -0.1225   0.0875  0.1225
419 rpp  0 0.9  -0.1575 -0.1225   0.0525  0.0875
420 rpp  0 0.9  -0.1575 -0.1225   0.0175  0.0525
421 rpp  0 0.9  -0.1575 -0.1225  -0.0175  0.0175
422 rpp  0 0.9  -0.1575 -0.1225  -0.0525 -0.0175
423 rpp  0 0.9  -0.1575 -0.1225  -0.0875 -0.0525
424 rpp  0 0.9  -0.1575 -0.1225  -0.1225 -0.0875
425 rpp  0 0.9  -0.1575 -0.1225  -0.1575 -0.1225
426 rpp  0 0.9  -0.1225 -0.0875  -0.1575 -0.1225
427 rpp  0 0.9  -0.0875 -0.0525  -0.1575 -0.1225
428 rpp  0 0.9  -0.0525 -0.0175  -0.1575 -0.1225
429 rpp  0 0.9  -0.0175  0.0175  -0.1575 -0.1225
430 rpp  0 0.9   0.0175  0.0525  -0.1575 -0.1225
431 rpp  0 0.9   0.0525  0.0875  -0.1575 -0.1225
432 rpp  0 0.9   0.0875  0.1225  -0.1575 -0.1225
c
501 rpp  0 0.9   0.1575  0.1925  -0.1925 -0.1575
502 rpp  0 0.9   0.1575  0.1925  -0.1575 -0.1225
503 rpp  0 0.9   0.1575  0.1925  -0.1225 -0.0875
504 rpp  0 0.9   0.1575  0.1925  -0.0875 -0.0525
505 rpp  0 0.9   0.1575  0.1925  -0.0525 -0.0175
506 rpp  0 0.9   0.1575  0.1925  -0.0175  0.0175
507 rpp  0 0.9   0.1575  0.1925   0.0175  0.0525
508 rpp  0 0.9   0.1575  0.1925   0.0525  0.0875
509 rpp  0 0.9   0.1575  0.1925   0.0875  0.1225
510 rpp  0 0.9   0.1575  0.1925   0.1225  0.1575
511 rpp  0 0.9   0.1575  0.1925   0.1575  0.1925
512 rpp  0 0.9   0.1225  0.1575   0.1575  0.1925
513 rpp  0 0.9   0.0875  0.1225   0.1575  0.1925
514 rpp  0 0.9   0.0525  0.0875   0.1575  0.1925
515 rpp  0 0.9   0.0175  0.0525   0.1575  0.1925
516 rpp  0 0.9  -0.0175  0.0175   0.1575  0.1925
517 rpp  0 0.9  -0.0525 -0.0175   0.1575  0.1925
518 rpp  0 0.9  -0.0875 -0.0525   0.1575  0.1925
519 rpp  0 0.9  -0.1225 -0.0875   0.1575  0.1925
520 rpp  0 0.9  -0.1575 -0.1225   0.1575  0.1925
521 rpp  0 0.9  -0.1925 -0.1575   0.1575  0.1925
522 rpp  0 0.9  -0.1925 -0.1575   0.1225  0.1575
```

```
523 rpp  0 0.9  -0.1925 -0.1575   0.0875  0.1225
524 rpp  0 0.9  -0.1925 -0.1575   0.0525  0.0875
525 rpp  0 0.9  -0.1925 -0.1575   0.0175  0.0525
526 rpp  0 0.9  -0.1925 -0.1575  -0.0175  0.0175
527 rpp  0 0.9  -0.1925 -0.1575  -0.0525 -0.0175
528 rpp  0 0.9  -0.1925 -0.1575  -0.0875 -0.0525
529 rpp  0 0.9  -0.1925 -0.1575  -0.1225 -0.0875
530 rpp  0 0.9  -0.1925 -0.1575  -0.1575 -0.1225
531 rpp  0 0.9  -0.1925 -0.1575  -0.1925 -0.1575
532 rpp  0 0.9  -0.1575 -0.1225  -0.1925 -0.1575
533 rpp  0 0.9  -0.1225 -0.0875  -0.1925 -0.1575
534 rpp  0 0.9  -0.0875 -0.0525  -0.1925 -0.1575
535 rpp  0 0.9  -0.0525 -0.0175  -0.1925 -0.1575
536 rpp  0 0.9  -0.0175  0.0175  -0.1925 -0.1575
537 rpp  0 0.9   0.0175  0.0525  -0.1925 -0.1575
538 rpp  0 0.9   0.0525  0.0875  -0.1925 -0.1575
539 rpp  0 0.9   0.0875  0.1225  -0.1925 -0.1575
540 rpp  0 0.9   0.1225  0.1575  -0.1925 -0.1575

c physics cards
cut:p j 0.010
cut:e j 0.010
phys:p 2j 1
imp:p 1 125r 0
imp:e 1 125r 0
mode p e
c
m2 71000 2 14000 1 8016 5
c m3 80000 1 53000 2    $ Mercury Iodide HgI2 rho = 6.36 g/cm3
m3 55000 1 53000 1    $ Cesium Iodide rho = 4.51 g/cm3
m4 14000 2 1001 6     $ Amorphous silicon rho = 2.35 g/cc
m5 14000 1 8000 2     $ glass rho = 2.18 g/cc
m6 13000 1              $aluminum rho = 2.70 g/cc
c
sdef sur=2 dir=1 vec=1 0 0  x=-3.2532 y=d3 z=d4   erg=0.1
c sc1  co60, erdtmann, 19985 gammas/dis
c si1  l .34695 .46720 .82618 1.17323 1.33251 2.15870 2.50575
c sp1    .0078  .00040 .00550  99.860  99.98   .0008  .000009
c
si3  -0.0175 0.0175
sp3  0 1
si4  -0.0175 0.0175
sp4  0 1
c
c tallies
f1:p 4
c1 0. 1.
c above is a probab check to make sure nothing is lost
c
c Charge deposition
+f8:pe  11 101 102 103 104 105 106 107 108
       201 202 203 204 205 206 207 208 209 210
       211 212 213 214 214 215 216
       301 302 303 304 305 306 307 308 309 310
       311 312 313 314 315 316 317 318 319 320
       321 322 323 324
       401 402 403 404 405 406 407 408 409 410
```

```
       411 412 413 414 415 416 417 418 419 420
       421 422 423 424 425 426 427 428 429 430 431 432
       501 502 503 504 505 506 507 508 509 510
       511 512 513 514 515 516 517 518 519 520
       521 522 523 524 525 526 527 528 529 530
       531 532 533 534 535 536 537 538 539 540   t
c
c Energy deposition
*f18:pe  11 101 102 103 104 105 106 107 108
       201 202 203 204 205 206 207 208 209 210
       211 212 213 214 214 215 216
       301 302 303 304 305 306 307 308 309 310
       311 312 313 314 315 316 317 318 319 320
       321 322 323 324
       401 402 403 404 405 406 407 408 409 410
       411 412 413 414 415 416 417 418 419 420
       421 422 423 424 425 426 427 428 429 430 431 432
       501 502 503 504 505 506 507 508 509 510
       511 512 513 514 515 516 517 518 519 520
       521 522 523 524 525 526 527 528 529 530
       531 532 533 534 535 536 537 538 539 540   t
c
c Charge deposition
+f28:pe  11 101 102 103 104 105 106 107 108
       201 202 203 204 205 206 207 208 209 210
       211 212 213 214 214 215 216
       301 302 303 304 305 306 307 308 309 310
       311 312 313 314 315 316 317 318 319 320
       321 322 323 324
       401 402 403 404 405 406 407 408 409 410
       411 412 413 414 415 416 417 418 419 420
       421 422 423 424 425 426 427 428 429 430 431 432
       501 502 503 504 505 506 507 508 509 510
       511 512 513 514 515 516 517 518 519 520
       521 522 523 524 525 526 527 528 529 530
       531 532 533 534 535 536 537 538 539 540   t
c
c Energy deposition
*f38:pe 11 101 102 103 104 105 106 107 108
       201 202 203 204 205 206 207 208 209 210
       211 212 213 214 214 215 216
       301 302 303 304 305 306 307 308 309 310
       311 312 313 314 315 316 317 318 319 320
       321 322 323 324
       401 402 403 404 405 406 407 408 409 410
       411 412 413 414 415 416 417 418 419 420
       421 422 423 424 425 426 427 428 429 430 431 432
       501 502 503 504 505 506 507 508 509 510
       511 512 513 514 515 516 517 518 519 520
       521 522 523 524 525 526 527 528 529 530
       531 532 533 534 535 536 537 538 539 540   t
nps 1e9
prdmp 2j 1
```

Appendix B

The 3-D detector blur plots for the "pen_rad" simulations.

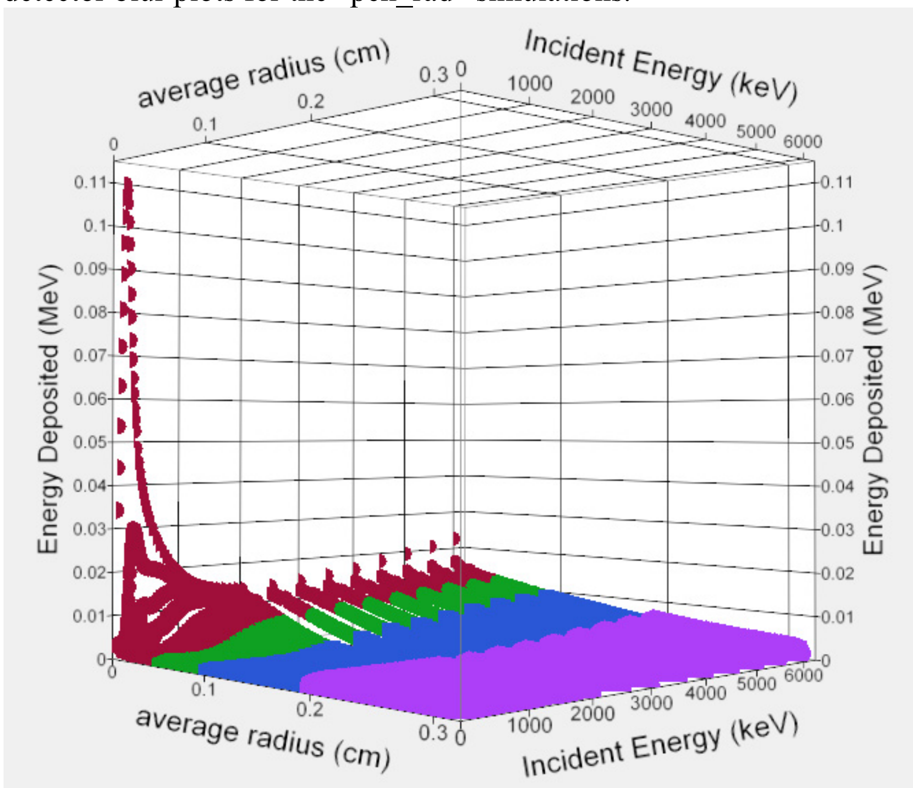

Figure 10 – First view of the pen_rad detector blur.

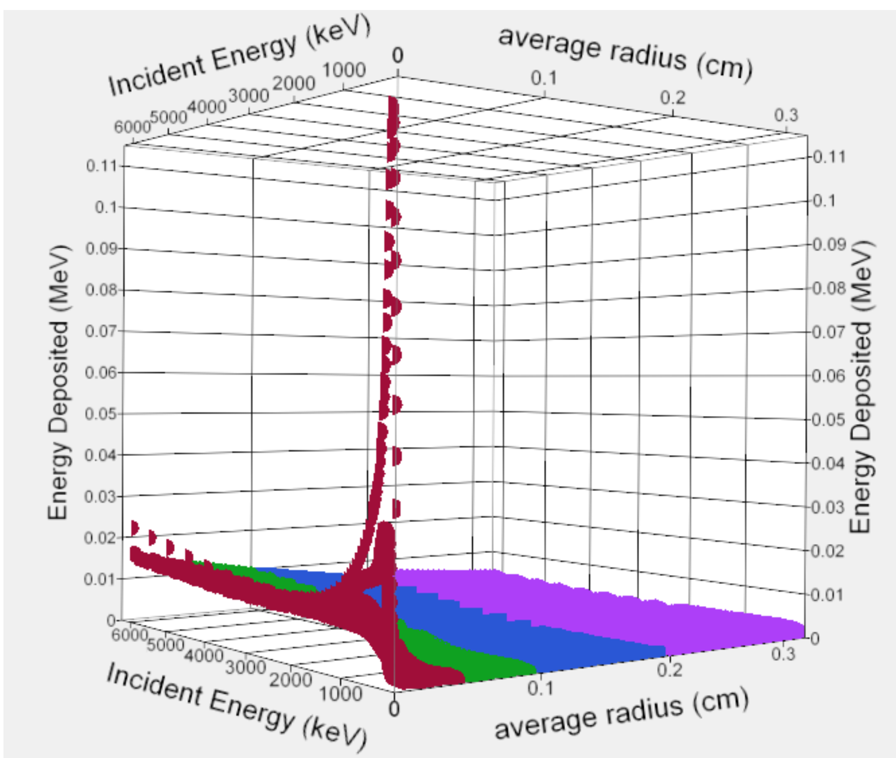

Figure 11 – Second view of the pen_rad detector blur.

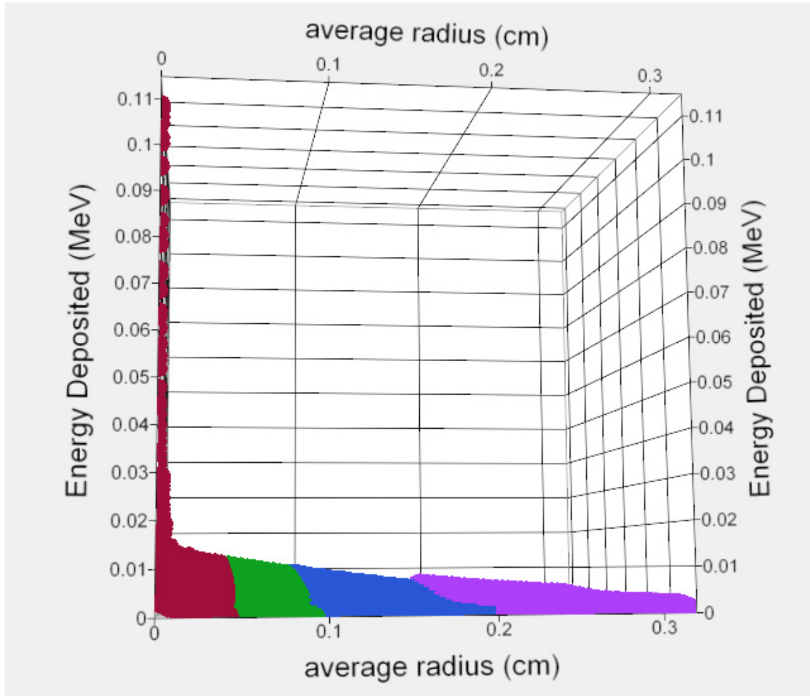

Figure 12 – View of the pen_rad detector blur along the incident energy axis.

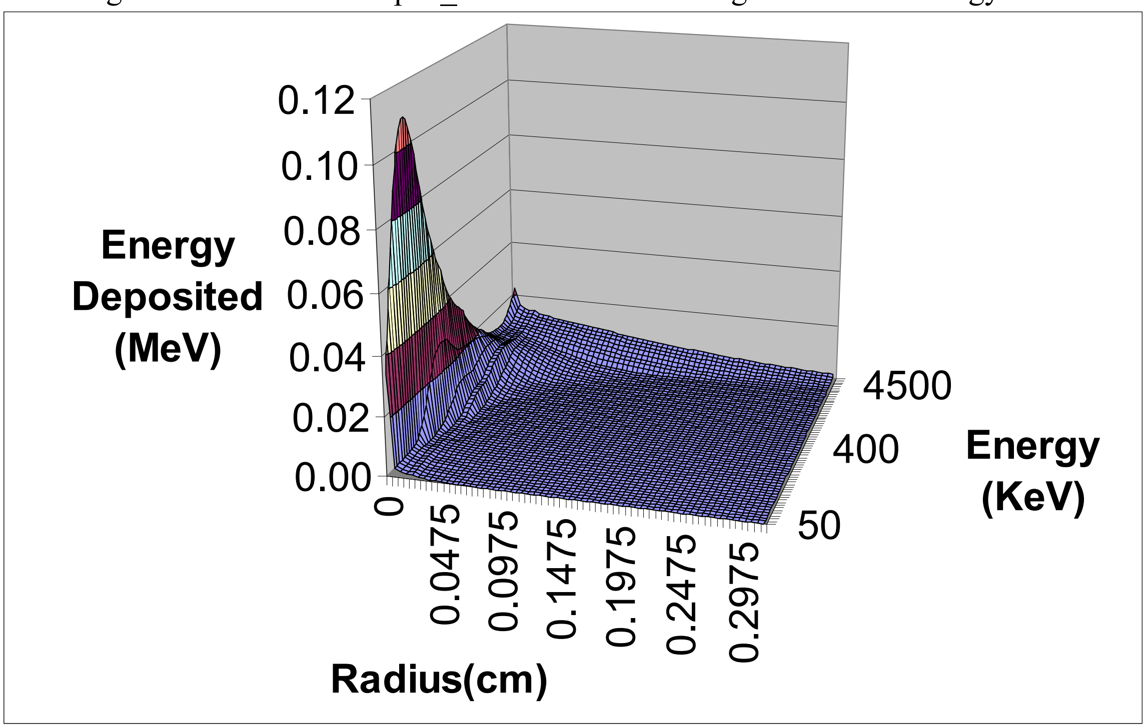

Figure 13 - 3-D EXCEL plot of the “pen_rad” detector blur.

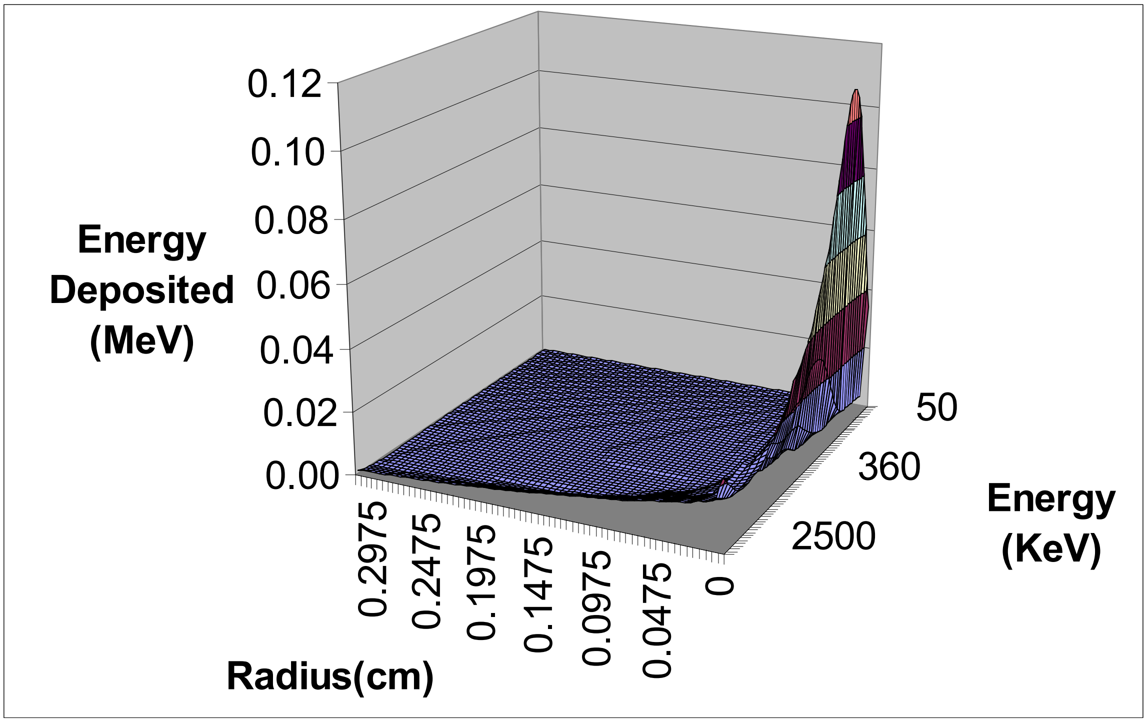

Figure 14 – 3-D EXCEL plot of the “pen_rad” detector blur.

Appendix C

The 3-D detector blur plots for the "pix_rad" simulations.

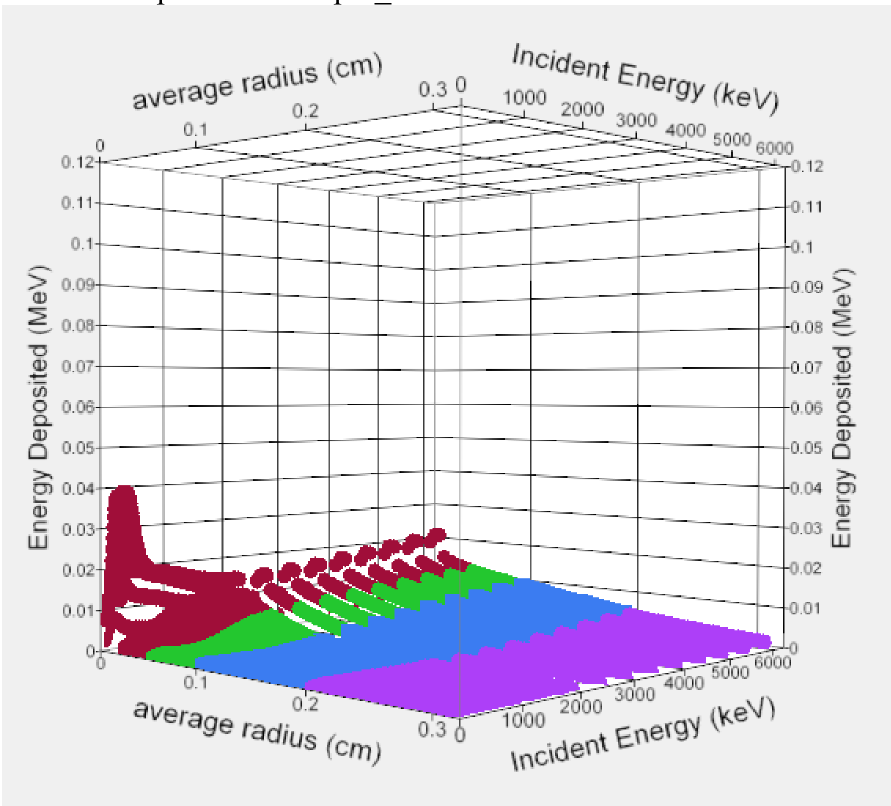

Figure 15- First view of the pix_rad detector blur.

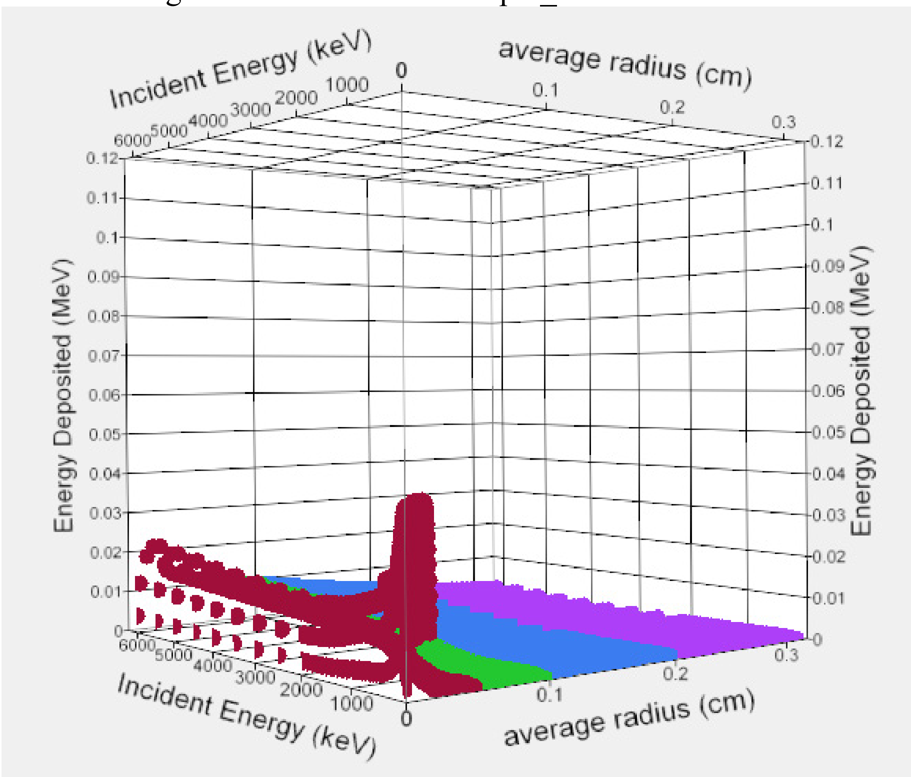

Figure 16 - Second view of the pix_rad detector blur.

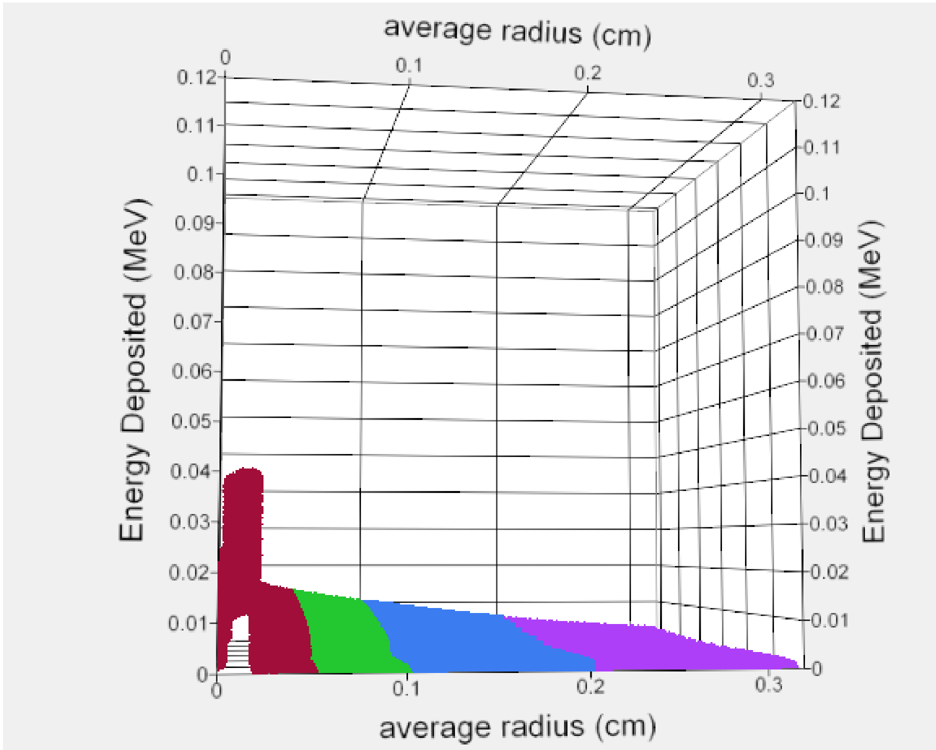

Figure 17 – View of the pix_rad detector blur along the incident energy axis.

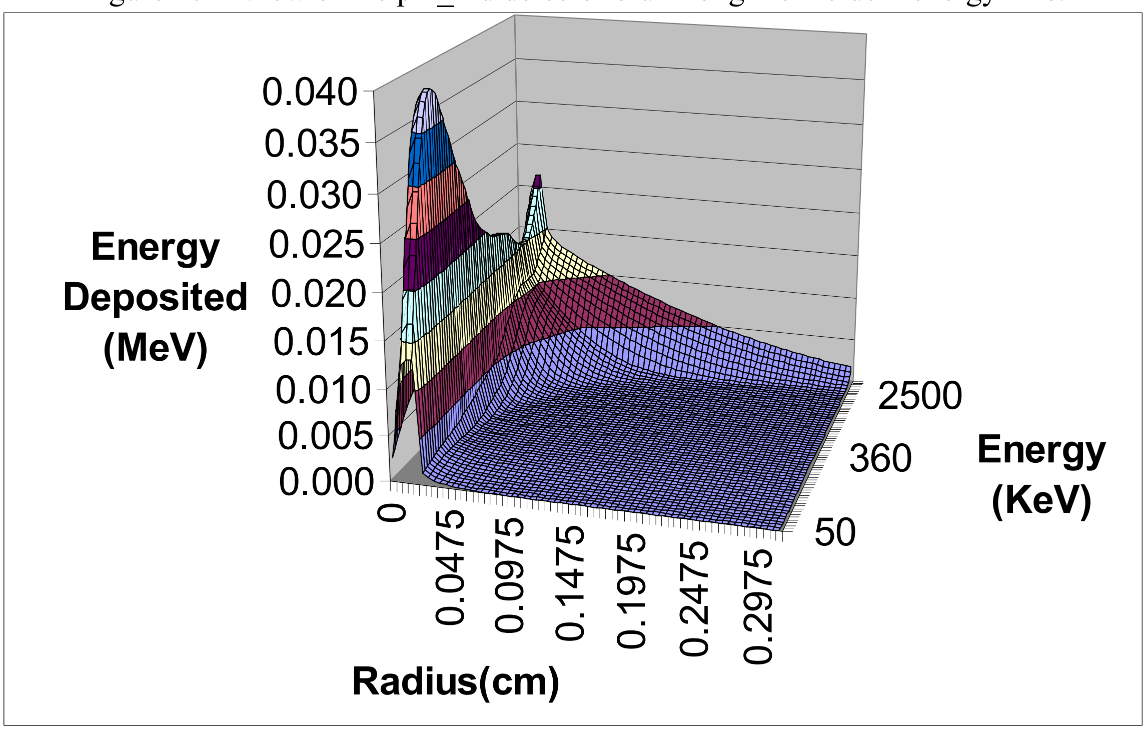

Figure 18 – 3-D EXCEL plot of ”pix_rad” detector blur.

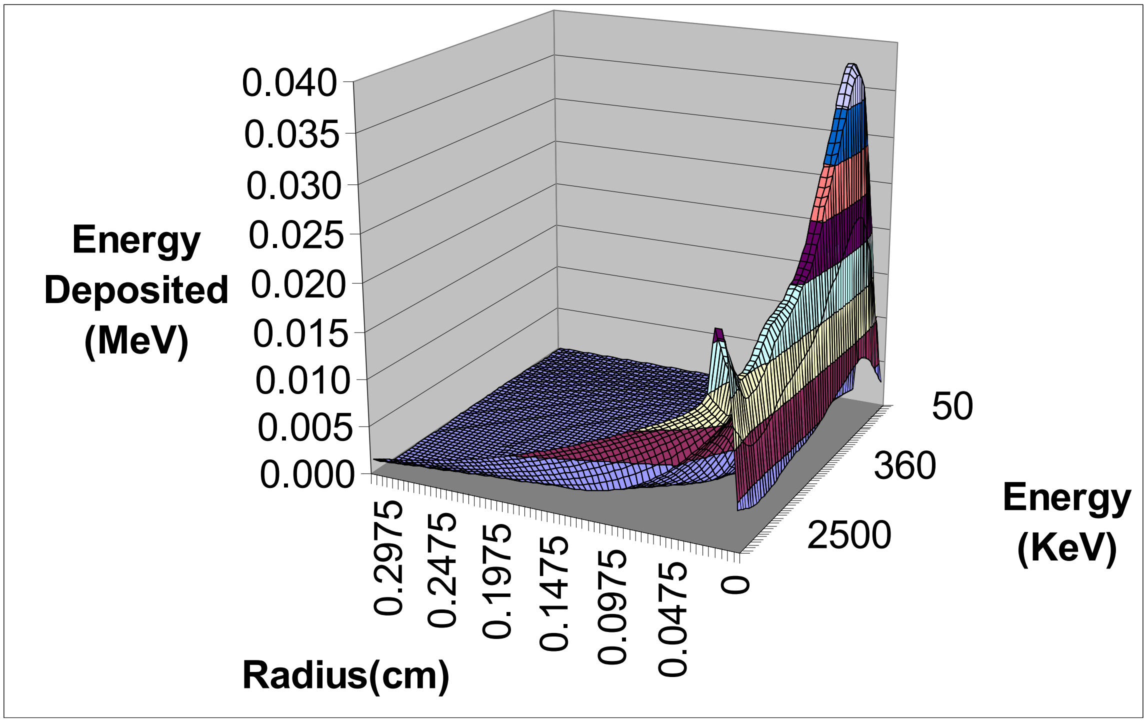

Figure 19 - 3-D EXCEL plot of “pix_rad” detector blur.

Appendix D

The 3-D detector blur plots for the "pix_pix" simulations.

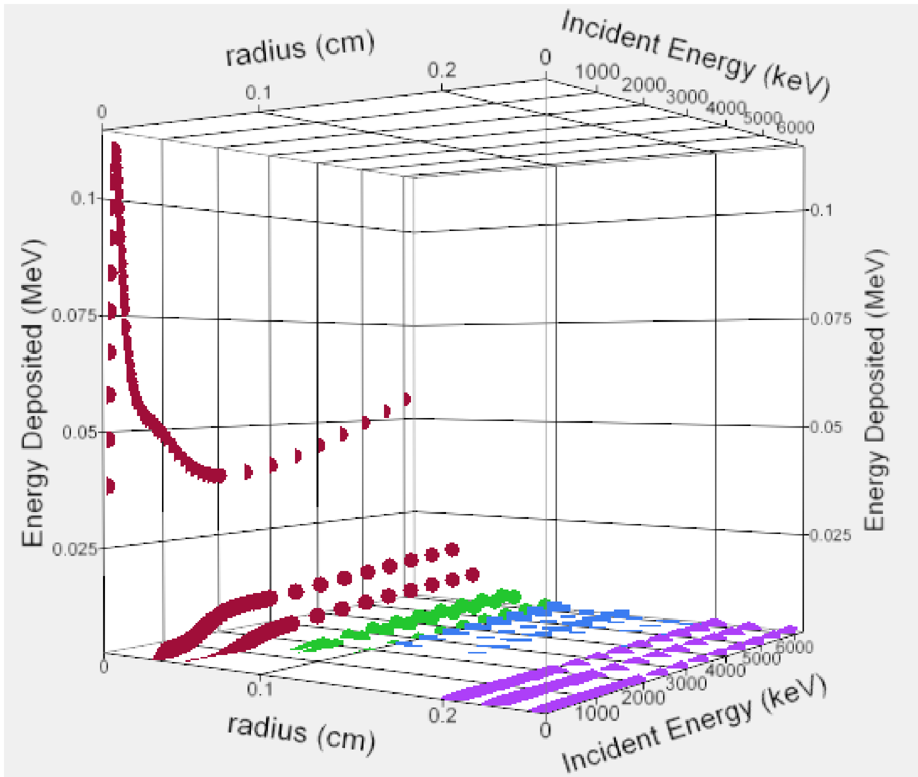

Figure 20 – First view of the pix_pix detector blur.

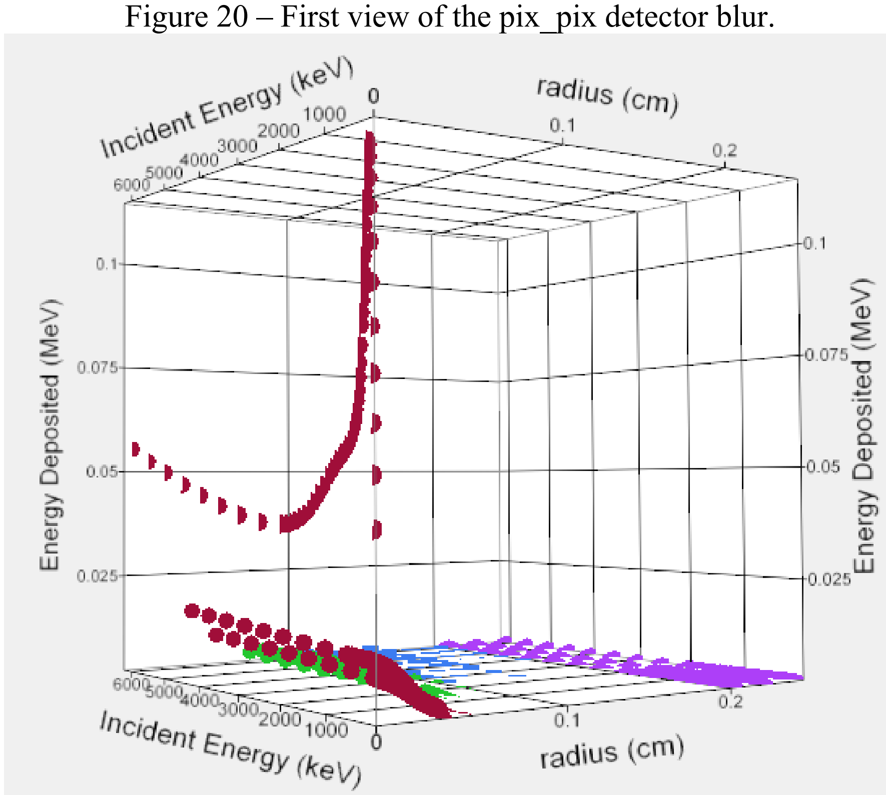

Figure 21 – Second view of the pix_pix detector blur.

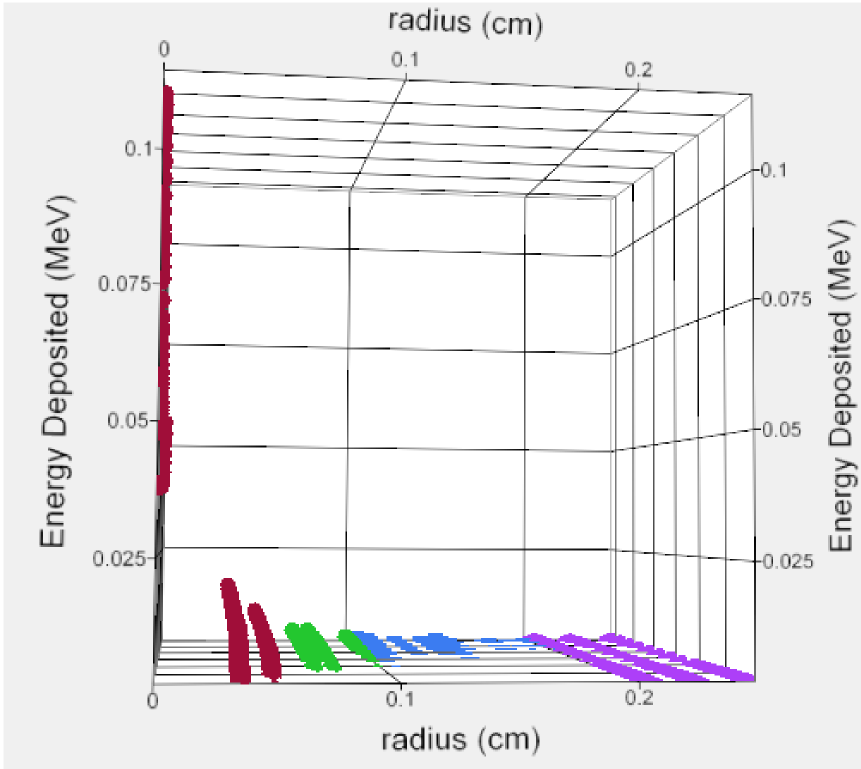

Figure 22 – View of the pix_pix detector blur along the incident energy axis.

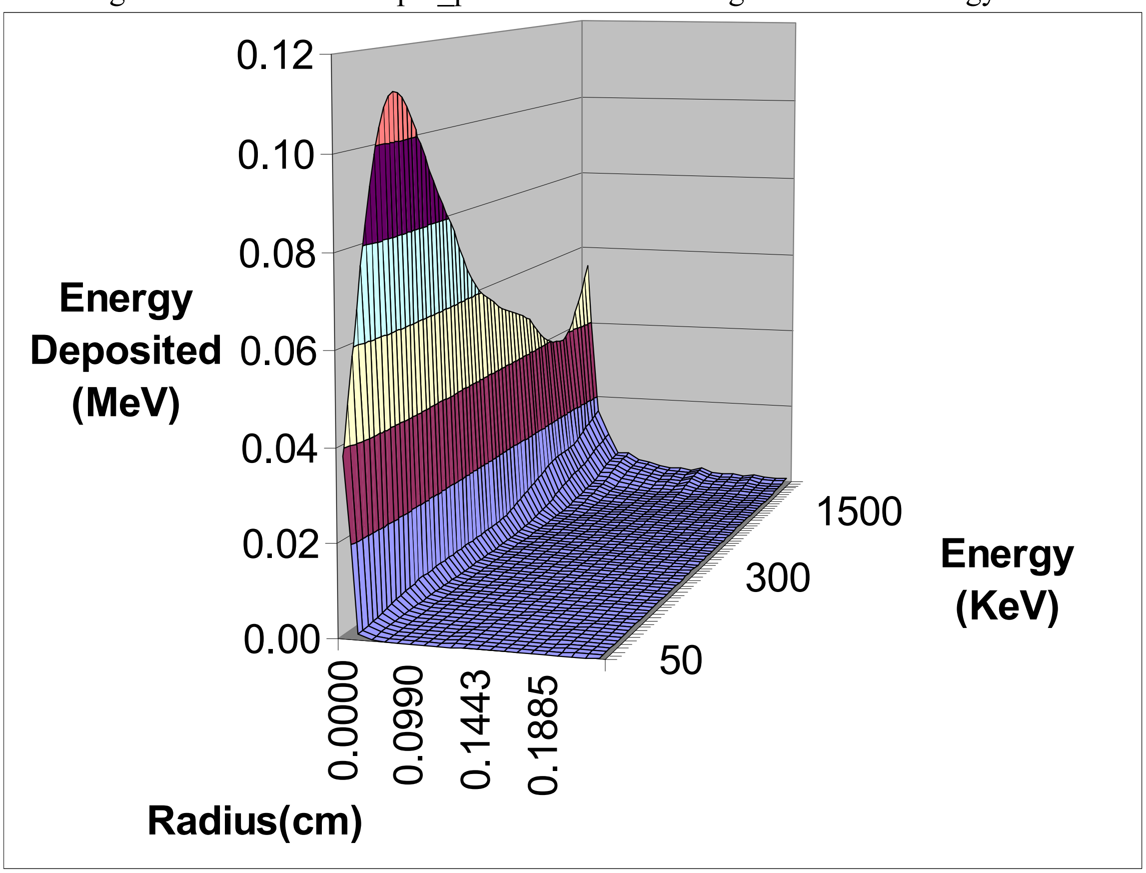

Figure 23- 3-D EXCEL plot of the "pix_pix" detector blur.

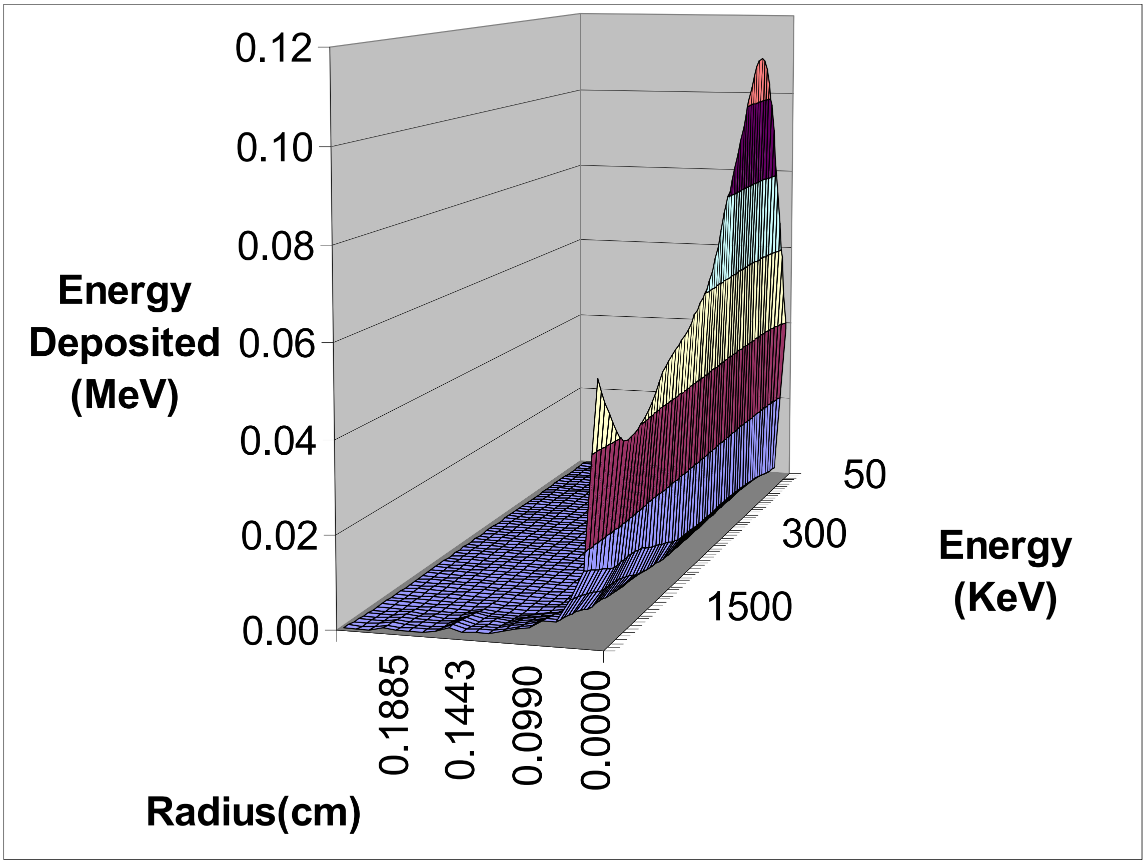

Figure 24 – 3-D EXCEL plot of the "pix_pix" detector blur.

Appendix E

The 3-D detector blur plots for the "pen_pix" simulations.

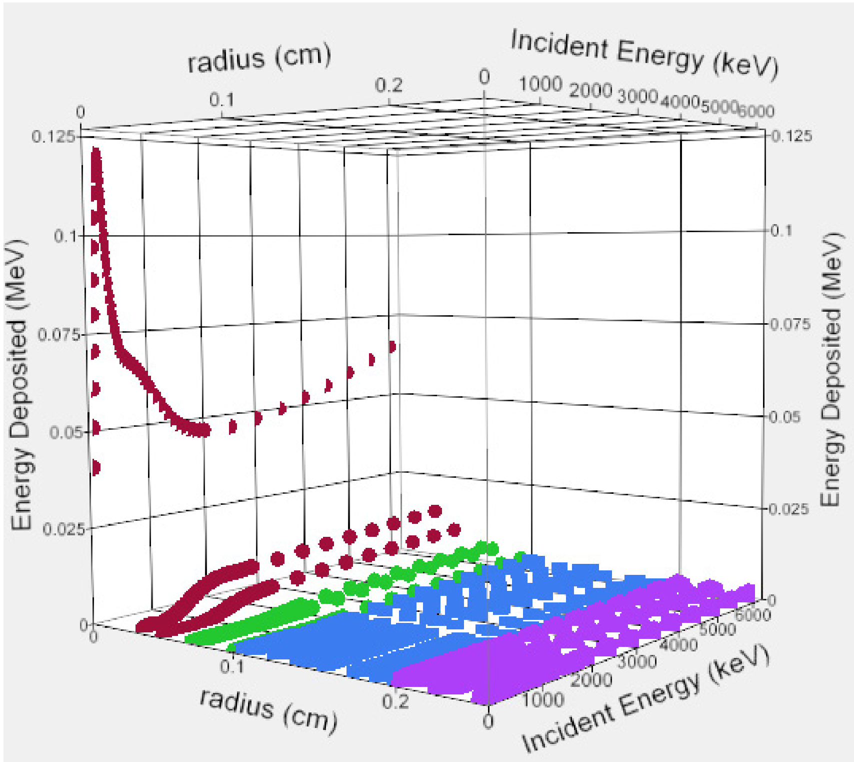

Figure 25 – First view of the pen_pix detector blur.

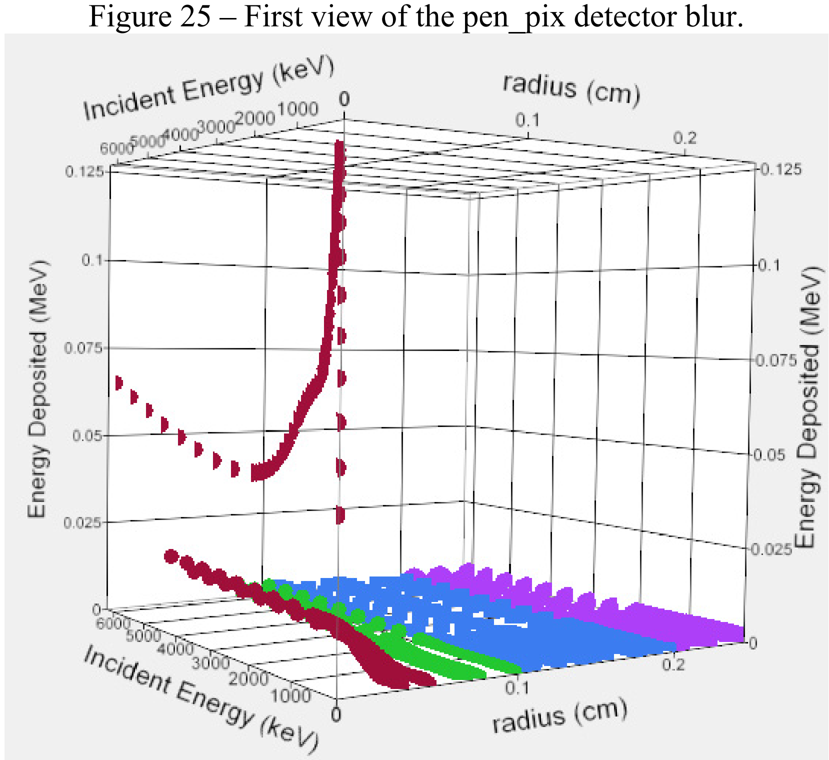

Figure 26 – Second view of the pen_pix detector blur.

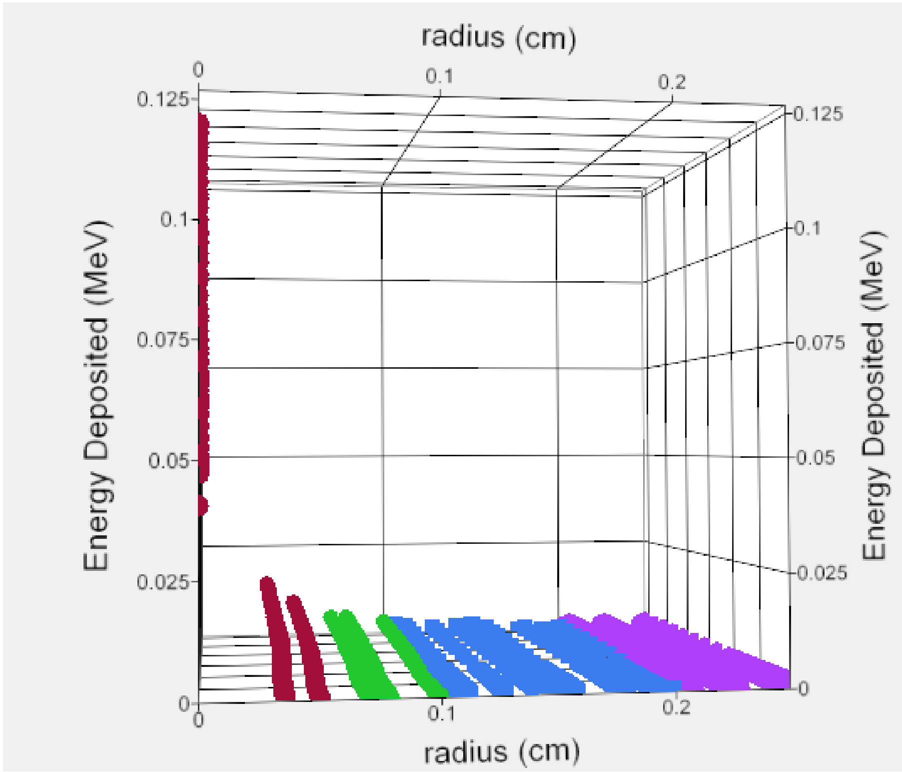

Figure 27 – View of the pen_pix detector blur along the incident energy axis.

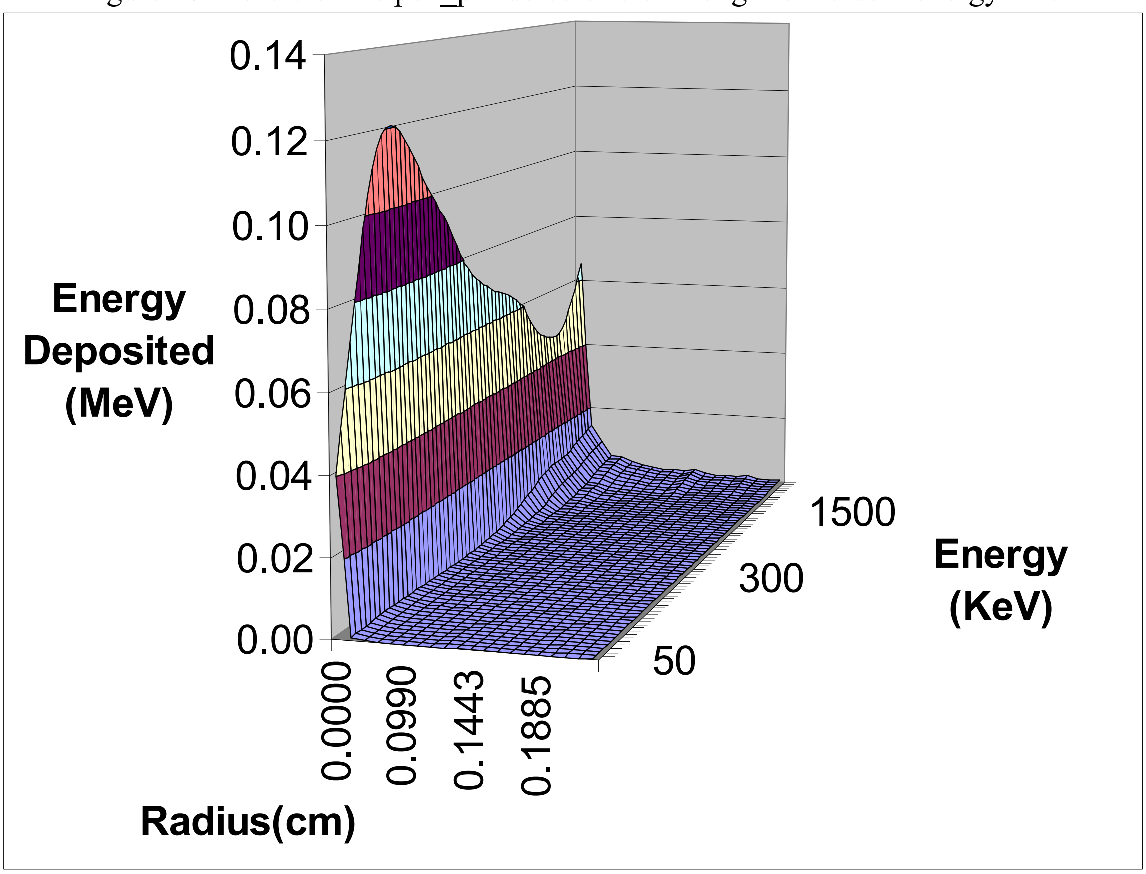

Figure 28 – 3-D EXCEL plot of the "pen_pix" detector blur.

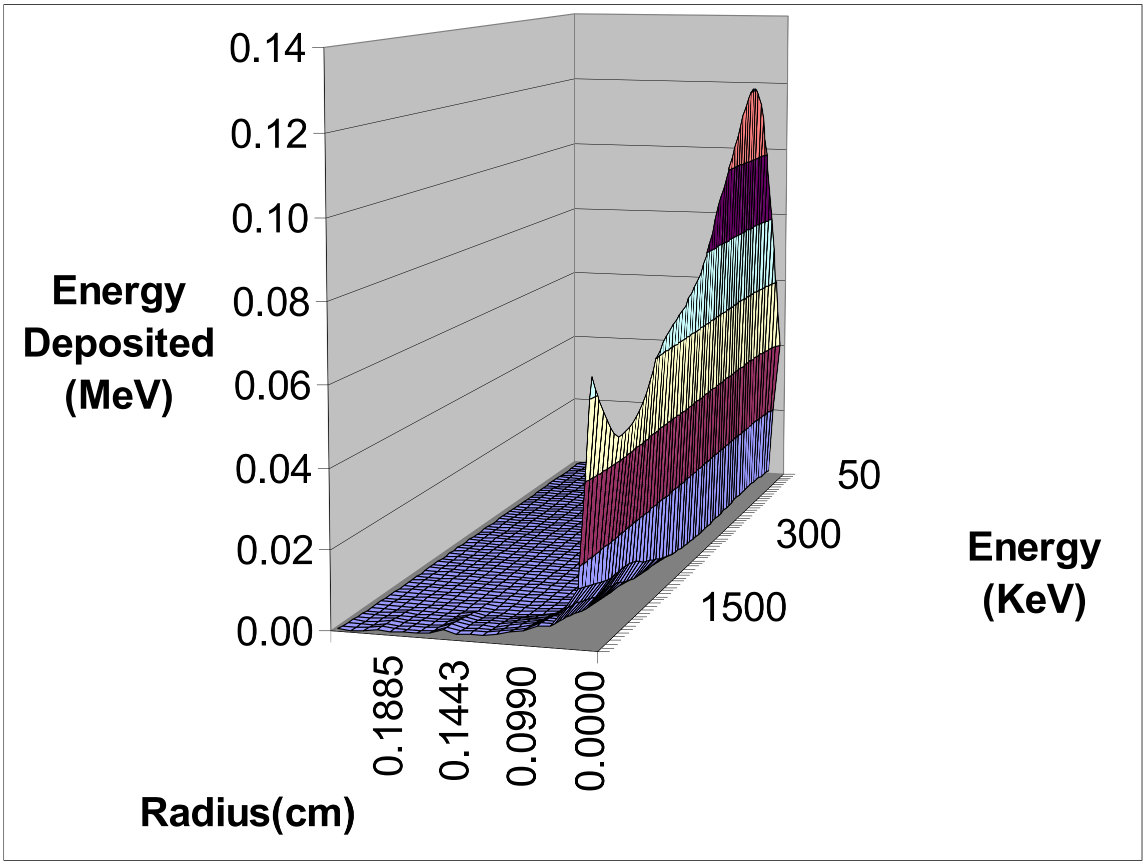

Figure 29- 3-D EXCEL plot of the "pen_pix" detector blur.

---

[1] Saint-Gobain Corp., "Bicron CsI Detctor Manual", plot obtained from Hans Snyder.
[2] Duane Flamig, Personal communication, November 2007.
[3] Avneet Sood, Personal communication, November 2007